UNIVERSITI MALAYSIA PERLIS

International Journal of Nanoelectronics and Materials

IJNeaM

ISSN 1985-5761 | E-ISSN 2232-1535

Structural, electronic, thermoelectric, and optical properties of anti-perovskite X_3SiO (X = Ba, Sr, Ca) using the first principle method

Muhammad Sholihin A. Rahim [a,b,c] *, Abdullah Chik [a,b,c], Yeoh Cheow Keat [a,b,c], Ishak Jainoo [c], and Nur Aina Syafarina [a,b,c]

[a]*Center for Frontier Materials Research, Universiti Malaysia Perlis, 01000 Kangar, Perlis, Malaysia*
[b]*Center of Excellence Geopolymer and Green Technology (CEGeoGTech), Universiti Malaysia Perlis (UniMAP), 02600 Jejawi, Arau, Perlis, Malaysia*
[c]*Faculty of Chemical Engineering & Technology, Taman Muhibah School Complex 2, 02600 Jejawi, Arau, Perlis, Malaysia*
* *Corresponding author. Tel.: +60175430797; e-mail: msholihin555@gmail.com*

Received 27 January 2026, Revised 27 May 2026, Accepted 5 June 2026

ABSTRACT

Anti-perovskite materials have unique structural and electronic properties that offer significant potential for thermoelectric and optical applications, mainly because of their direct gap semiconducting behavior. In this work, we investigate the structural, electronic, thermoelectric, and optical properties of anti-perovskite X_3SiO (X = Ba, Sr, Ca) using the density functional theory (DFT) method. These properties were computed by employing the generalized gradient approximation with the Perdew-Burke-Ernzerhof (GGA-PBE) exchange-correlation function. The structural, electronic, and optical properties were calculated using the CASTEP code, while thermoelectric properties were calculated using the BoltzTraP code that utilized the Boltzmann transport equation (BTE). Our analysis of band structure for Ba_3SiO, Sr_3SiO, and Ca_3SiO shows that these materials have direct band gaps with semiconducting behavior at Γ-Γ k-points. The band gap values are 0.44 eV, 0.43 eV, and 0.11 eV for Ba_3SiO, Sr_3SiO, and Ca_3SiO respectively. The elastic property analysis indicates that all three compounds are brittle due to their Pugh's ratio $\leqq 0.5$. Furthermore, the thermoelectric analysis revealed that Ba_3SiO and Sr_3SiO compounds are n-type materials, while the Ca_3SiO compound is a p-type material at 300 K. However, our results show that anti-perovskite X_3SiO (X = Ba, Sr, Ca) exhibits relatively poor thermoelectric performance with low figure of merit (*ZT*) values of 9.66×10^{-4}, 9.59×10^{-4}, and 2.50×10^{-2} for Ba_3SiO, Sr_3SiO, and Ca_3SiO, respectively, at room temperature. Regarding optical properties, these compounds have a wide absorption spectrum from 0 eV to 30 eV, from the infrared to the ultraviolet region. The maximum peaks in reflection coefficient were observed in the high ultraviolet light energy range (>20 eV), suggesting that Ba_3SiO, Sr_3SiO, and Ca_3SiO are excellent reflectors.

Keywords: *Density functional theory, Anti-perovskite, Thermoelectric properties, Optical properties, Semiconductor materials*

1. INTRODUCTION

Anti-perovskites are a class of structural compounds characterized by an atomic arrangement in which cations and anions occupy inverted positions compared to perovskite materials, while still retaining a perovskite crystal structure [1]. The general chemical formula of anti-perovskite is X_3AB, where A and B are anions and X is a cation. Over the past decade, there has been increasing interest in anti-perovskite materials due to their potential in various applications, particularly in energy conversion [2], the technology that can convert waste heat into electrical current [3].

Anti-perovskites containing alkaline metals, transition metals, and alkaline earth metals for X cations have been widely investigated because of their electronic and transport properties [4]. Their semiconducting nature makes anti-perovskite compounds suitable candidates for thermoelectric and optical applications [5]. In particular, anti-perovskite compounds that composed alkaline-earth metals combined with group 14 elements have demonstrated favorable semiconducting behavior [6]. Recent studies have highlighted the strong thermoelectric potential of Ba_3SiO and Ba_3GeO compounds. For example, He *et al.* investigated thermoelectric properties of Ba_3SiO and Ba_3GeO compounds using Heyd-Scuseria-Ernzerhof (HSE). He *et al.* reported that Ba_3SiO exhibits a higher figure of merit with the value of 2.14 at 600 K compared to Ba_3GeO [7]. This result indicates that Ba_3SiO is a promising material for thermoelectric applications.

In addition to thermoelectric performance, optical properties play a role in determining the applicability of semiconductors in optoelectronic and photovoltaic devices. Materials with direct band gaps are generally considered ideal for optical applications due to their ability to absorb light efficiently. For example, $ANSr_3$ (A = As, Sb, Bi) compounds have been identified as probable candidate materials for optical applications because these compounds show direct band gaps [8]. Similarly, the simulation study on Ba_4As_3O and Ba_4Sb_3O has confirmed their suitability for photovoltaic applications. These compounds show direct band gaps of 1.1 eV and 1.3 eV for Ba_4As_3O and Ba_4Sb_3O, respectively, which enable strong absorption of visible light [9]. Furthermore, the thermoelectric and optical properties of A_3SnO (A = Ca, Sr, Ba) have been investigated using the full-potential linearized augmented plane wave (FP-LAPW) method. These three compounds were reported to be direct band gap semiconductors with band gap values of 0.51 eV, 0.48 eV, and 0.10 eV for Ca_3SnO, Sr_3SnO, and Ba_3SnO, respectively, highlighting their suitability as good candidates for both optical and thermoelectric applications [10].

Mahmood *et al.* further explored the physical properties of anti-perovskite Ca_3XO (X = Si, Ge) in both cubic (Pm-3m) and orthorhombic (Pbnm) crystal structures using a modified Becke and Johnson (mbJ) approach [11]. Their results showed that Ca_3SiO and Ca_3GeO exhibit narrow band gap semiconducting behavior with the band gap values of 0.91 eV and 0.89 eV for the cubic structure and approximately 0.70 eV and 0.73 eV for the orthorhombic structure, respectively. Although extensive studies have focused on cubic anti-perovskite nitrides, oxides, and carbides; however, orthorhombic anti-perovskite oxides remain relatively underexplored within the anti-perovskite family [12]. Moreover, existing literature suggests that structural transition from cubic to orthorhombic can improve the thermoelectric properties of anti-perovskite materials. Despite this potential advantage, most previous literature has been limited in addressing the orthorhombic oxide structure for thermoelectric applications [13].

As discussed above, the thermoelectric properties of Ba_3SiO and Ca_3SiO compounds have been reported, but for Sr_3SiO, it remains unexplored. In addition to their thermoelectric properties, anti-perovskites also hold great promise for optical applications. Moreover, to date, the research on the optical properties of Ba_3SiO, Ca_3SiO, and Sr_3SiO compounds has not been examined. So, in this work, we investigated the structural, electronic, thermoelectric, and optical properties of anti-perovskite X_3SiO (X = Ba, Sr, Ca) in an orthorhombic crystal structure using the density functional theory (DFT) method.

2. COMPUTATIONAL DETAILS

The simulation study was conducted on the orthorhombic crystal structures of Imma (No. 16) for Ca_3SiO and Pnma (No. 62) for both Ba_3SiO and Sr_3SiO. The density functional theory (DFT) method was utilized to calculate the structural, electronic, thermoelectric, and optical properties of anti-perovskite X_3SiO (X = Ba, Sr, Ca) using generalized gradient approximation with the Perdew-Burke-Ernzerhof (GGA-PBE) [14] along with an on-the-fly-generated (OTFG) ultra-soft pseudopotential. The parameter optimization was performed to obtain optimized k-point and energy cut-off. The optimized k-point for Brillouin zone sampling was chosen at 5 × 5 × 3, 5 × 5 × 4, and 4 × 4 × 3, while the plane wave energy cut-off was established at 600 eV for Ba_3SiO, and 700 eV for Sr_3SiO and Ca_3SiO. The geometry optimization was then performed to obtain a stable structure of X_3SiO (X = Ba, Sr, Ca) using the Bryoden-Fletcher-GoldFarb-Shanno (BFGS) method. The final convergence of geometry optimization was achieved with a tolerance value of 5×10^{-5} eV/atom for total energy per atom, 2×10^{-1} eV/Å for maximum residual force, 1×10^{-3} Å for maximum atom displacement, and 0.2 eV/Å for maximum allowed ionic (force) on an atom.

After achieving convergence, the structural, electronic, and optical properties were calculated using the Cambridge Serial Total Energy Program (CASTEP) code [15], whereas the thermoelectric properties were computed using the Boltzmann transport equation (BTE) that was implemented in the Boltzmann Transport Properties (BoltzTraP) code [16]. All thermoelectric properties are calculated over the temperature range of 300 K to 1000 K. Furthermore, the elastic properties were calculated using finite strain theory. This approach describes the relationship between stress and strain in materials under deformation. The elastic constants serve as the proportionality factors between the applied strain and resulting stress. Hence, this relationship is expressed as $\sigma_i = C_{ij}\varepsilon_j$, where σ_i represents the stress, ε_j is the strain, and C_{ij} is the elastic constant that connects them. The bulk modulus (B) and shear modulus (G) were computed from C_{ij} using the Voigt-Reuss-Hill approximation [17]. In addition, the Young's modulus (E), which determines the stiffness of materials, is calculated using $E = (9GB)/(3B + G)$. Finally, the optical properties were derived utilizing the Kramers-Kroning relation. The mathematical formulations used to calculate thermoelectric and optical properties are presented in their respective subsections.

3. RESULTS AND DISCUSSIONS

3.1. Structural Properties

The crystal structures of X_3SiO (X = Ba, Sr, Ca) are depicted in Figure 1. These compounds comprise three types of atoms: four oxygen (O) atoms, four silicon (Si) atoms, and 12 alkaline earth metal atoms, specifically barium (Br) atoms, strontium (Sr) atoms, and calcium (Ca) atoms. Generally, these structures exist at room temperature [18]. From structural analysis, the lattice parameters of Ba_3SiO were determined as a = 7.525 Å, b = 7.802 Å, and c = 10.838 Å, which is in good agreement with experimental values of a = 7.532 Å, b = 7.585 Å, c = 10.724 Å with space group Pnma (No. 62) [19]. In the case of Sr_3SiO, the lattice parameters were determined to be a = 7.159 Å, b = 7.200 Å and c = 10.153 Å. These values show good agreement with the experimental values of a = 7.125 Å, b = 7.116 Å, and c = 10.074 Å for space group Pbnm (No. 4) [20]. Likewise, for Ca_3SiO, the lattice parameters were a = 6.667 Å, b = 6.686 Å, and c = 9.444 Å, which is in good agreement with theoretical values of a = 6.660 Å, b = 6.640 Å, and c = 9.400 Å [11]. The lattice parameter of these compounds shows a decreasing trend from Ba^{2+} to Sr^{2+} to Ca^{2+}, which correlates with the difference in X cation radius size of these atoms.

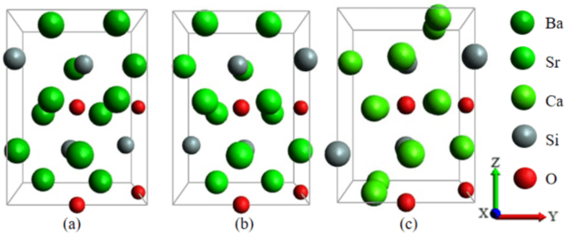

Figure 1. Crystal structure of (a) Ba_3SiO, (b) Sr_3SiO, and (c) Ca_3SiO

For structural analysis, Ba_3SiO shows the largest lattice parameter and cell volume (640.44 Å^3) due to large ionic radius of Ba^{2+} (1.35 Å) [21]. In comparison, Sr_3SiO with smaller ionic radius of Sr^{2+} (1.18 Å) [21] has lower lattice parameters and cell volume (523.32 Å^3) while Ca_3SiO, which contains the smallest ionic radius of Ca^{2+} (1.00 Å) [21] shows the smallest lattice parameter and cell volume (421.02Å^3). This trend demonstrates that the variations in the ionic radii size of X cations highly influence the lattice parameter and cell volume of Ba_3SiO, Sr_3SiO, and Ca_3SiO compounds. Furthermore, the higher atomic weight of Ba^{2+} (137.33 g/mol) contributes to the greater molecular density of 4.72 g/cm^3 in Ba_3SiO, compared to Sr^{2+} (87.6 g/mol) in Sr_3SiO with a molecular density of 3.89 g/cm^3 and Ca^{2+} (40.08 g/mol) in Ca_3SiO with a molecular density of 2.59 g/cm^3. As the atomic weight of the X cation decreases from Ba^{2+} to Sr^{2+} to Ca^{2+}, the molecular density of Ba_3SiO, Sr_3SiO, and Ca_3SiO compounds also decreases accordingly.

Table 1 shows the calculated Young's modulus and bulk modulus of the Ba_3SiO, Sr_3SiO, and Ca_3SiO compounds. These compounds display a high Young's modulus (E) and low bulk modulus (B). A high Young's modulus indicates that these compounds are stiff and resist deforming under compression and tension forces. However, their low bulk modulus shows that these compounds can be compressed under certain high, uniform pressures. Among these compounds, Ca_3SiO exhibits the highest values for both moduli compared to Ba_3SiO and Sr_3SiO. These results can be attributed to the shorter bond length of Ca_3SiO compared to Ba_3SiO and Sr_3SiO. The shortest bond length indicates a closer arrangement of atoms, which leads to stronger interatomic forces between atoms and ionic bonding in between Ca and O in Ca_3SiO. In contrast, the longer bond length in Ba_3SiO leads to a weaker interatomic force and lower bulk modulus. From elastic analysis, the substitution of X cation with different radius sizes shows increasing trend of Young's and bulk modulus from Ba^{2+} to Sr^{2+} to Ca^{2+}. To the best of our knowledge, there is no available data for experimental and theoretical studies for comparison of the elastic properties of these compounds. As such, this study can be baseline data that may guide future study of Ba_3SiO, Sr_3SiO, and Ca_3SiO compounds.

Pugh's ratio (B/G) is used to assess the ductility and brittleness of material. A material is considered brittle if the ratio is less than 1.75, while if the ratio is larger than 1.75, then the material is considered ductile. The calculated Pugh's ratio of Ba_3SiO, Sr_3SiO, and Ca_3SiO is 1.45, 1.25, and 1.18, respectively, classifying all three compounds as brittle materials since their B/G ratios are less than 1.75. Moreover, the lower B/G ratios are also related to the higher hardness, following the trend that increased from Ba^{2+} to Sr^{2+} to Ca^{2+}.

Table 2 presents the Mulliken bond population analysis for Ba_3SiO, Sr_3SiO, and Ca_3SiO compounds. Among these compounds, Ba_3SiO exhibits the longest bond distance of Ba–O at 2.779 Å compared to Sr–O with the bond distance of 2.581 Å in Sr_3SiO and Ca–O with the bond distance of 2.371 Å in Ca_3SiO. These results show that the longer bond distance in Ba_3SiO is attributed to the larger ionic radius size of Ba^{2+} compared to Sr^{2+} and Ca^{2+}. As the ionic radii size of X cations of these compounds increased, the attraction between the nucleus and outer electrons weakened, leading to a reduction in the electronegativity of the ions. The decrease in electronegativity disrupts the balance between the ionic X cation and oxygen atoms. As a result, the bond length increases, while the bond strength decreases.

Table 1. Calculated Young's modulus and bulk modulus of Ba_3SiO, Sr_3SiO, and Ca_3SiO (current study)

Compound	Space group	Method	Young's modulus, E (GPa)	Bulk modulus, B (GPa)
Ba_3SiO				
GGA-PBE	Pnma (No.62)	Theory (CASTEP)	96.35	33.86
Sr_3SiO				
GGA-PBE	Pnma (No.62)	Theory (CASTEP)	146.51	44.92
Ca_3SiO				
GGA-PBE	Imma (No.74)	Theory (CASTEP)	202.56	58.94

Table 2. Mulliken population analysis of Ba_3SiO, Sr_3SiO, and Ca_3SiO

Compound	Species	Mulliken charge	Bond lengths, Å	Bond population
Ba_3SiO	Ba	0.63	Ba–Ba = no bonding	-
	Si	−0.95	Si–Ba = no bonding	-
	O	−0.95	O–Ba = 2.779	0.14
Sr_3SiO	Sr	0.67	Sr–Sr = no bonding	-
	Si	−1.06	Si–Sr = no bonding	-
	O	−0.96	O–Sr = 2.581	0.15
Ca_3SiO	Ca	0.79	Ca–Ca = no bonding	-
	Si	−1.36	Si–Ca = no bonding	-
	O	−0.92	O–Ca = 2.366	0.16

In Mulliken population analysis [22], the bond population help to determine the bonding interaction and charge distribution in molecular compounds. The positive bond population values correspond to the bonding interactions, while the negative values are correlated with anti-bonding interactions. In compound formation, the Ba_3SiO, Sr_3SiO, and Ca_3SiO compounds are formed when two electrons are transferred from Ba, Sr, and Ca atoms, resulting in positive Ba^{2+}, Sr^{2+}, Ca^{2+} ions, while O atoms receive these electrons to become negative O^{2-} ions. The bond populations value can also show the chemical bonding of a compound. If the bond population value is below 0.5, this indicates ionic bonding existence, while if the value is above 0.5, this implies the presence of covalent bonding. In this study, the majority of anti-perovskite X_3SiO (X = Ba, Sr, Ca) compounds exhibit ionic bonding, as indicated by Mulliken bond population below 0.5. The positive bond population values also confirm the presence of bonding interactions between Ba–O, Sr–O, and Ca–O in Ba_3SiO, Sr_3SiO, and Ca_3SiO compounds, respectively.

Figure 2 shows the electron density distribution for Ba_3SiO, Sr_3SiO and Ca_3SiO compounds. In this mapping, the bond interaction of Ba–O, Sr–O, and Ca–O exhibits ionic bonding, as evidenced by the spherical electron charge distribution around Ba, Sr, Ca, and O atoms. These results are consistent with the finding from Mulliken bond population analysis that is presented in Table 2, further confirming the presence of ionic character of Ba–O, Sr–O, and Ca-O in Ba_3SiO, Sr_3SiO, and Ca_3SiO compounds, respectively.

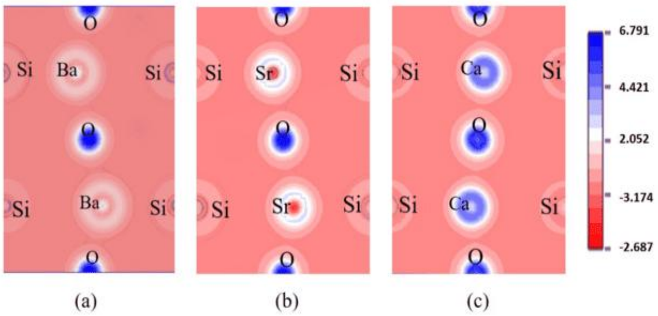

Figure 2. Electron density distribution mapping of (a) Ba_3SiO, (b) Sr_3SiO, and (c) Ca_3SiO

3.2. Electronic Properties

3.2.1. Band Structure Analysis

The high symmetry k-points at Γ − Y − T − Z − Γ − X − S − Y were used as sampling points in the first Brillouin zone for the band structure calculations of the Ba_3SiO, Sr_3SiO, and Ca_3SiO compounds. These band structures were computed using generalized gradient approximation with the Perdew-Burke-Ernzerhof (GGA-PBE) functional. The Fermi level is set at 0 eV in the band structure plot, which separates the valence band (blue lines) and conduction band (yellow lines). The calculated band structures for X_3SiO (X = Ba, Sr, Ca) are presented in Figure 3. From this figure also, the maximum of the valence band curve aligns with the minimum of the conduction band curve at Γ–Γ k-points, thus confirming that X_3SiO (X = Ba, Sr, Ca) compounds exhibit direct band gap semiconducting behavior. The calculated band gap values were found to be 0.44 eV, 0.43 eV, and 0.11 eV for Ba_3SiO, Sr_3SiO, and Ca_3SiO respectively, as shown in Table 3. The trend in band gap values decreases from Ba_3SiO, Sr_3SiO, and Ca_3SiO as the substitution of the X cation with different radius sizes from Ba^{2+} to Sr^{2+} to Ca^{2+}. This suggests the possibility of tuning the band gap by replacing the different X cation. According to Amin *et al.*, materials with a direct band gap are particularly advantageous for photonic and optoelectronic applications [23]. From this electronic property analysis, we assume these compounds are a good indicator to study for their optical property in order to determine the potential of these compounds for optical applications.

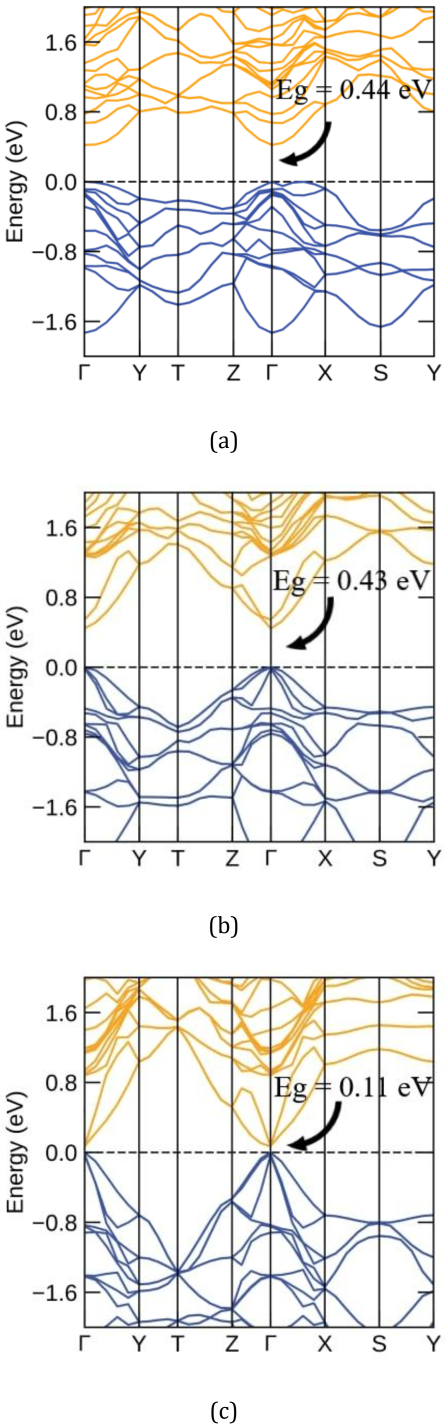

Figure 3. Band structure of (a) Ba_3SiO, (b) Sr_3SiO, and (c) Ca_3SiO

Table 3. Calculated band gap for Ba_3SiO, Sr_3SiO, and Ca_3SiO

Compound	Functional (XC)	Method	Energy gap (eV)
Ba_3SiO	GGA-PBE (current study)	Theory (CASTEP)	0.44
Sr_3SiO			0.43
Ca_3SiO			0.11
Ba_3SiO [24]	GGA-PBEsol	Theory (VASP)	0.42
Ca_3SiO [25]	GGA-PBE	Theory (VASP)	0.20

The calculated band structures in this study show good agreement with computational studies, particularly in confirming the direct band gap semiconducting behavior of these compounds. For instance, Garcia-Castro *et al.* reported a band gap of 0.42 eV for Ba_3SiO with space group (Pbnm, No. 62) using generalized gradient approximation with Perdew-Burke-Ernzerhof for solid (GGA with PBEsol) functional [24], and Pohls & Mar found a band gap of 0.20 eV for Ca_3SiO with space group (Imma, No. 74) using generalized gradient approximation with Perdew-Burke-Ernzerhof (GGA-PBE) [25]. The slightly higher band gap reported by Pohls & Mar compared to our result for Ca_3SiO is probably due to the author using different DFT code, the Vienna Ab initio Simulation Package (VASP), along with the projector augmented wave (PAW) method. We expected the different treatment of the basic set of these methods to be the root reason for this case. Based on previous literature, Ahmed Adllan and Dal Corso also reported that the difference between two results obtained using pseudopotential and PAW can be related to the difference in implementation of localized basis sets in these methods [26]. From the band structure analysis, the flat or nearly non-dispersing bands are determined in the valence band between Y and Z k-points for Ba_3SiO and between X and Y k-points for both Sr_3SiO and Ca_3SiO. These non-dispersion bands are correlated with localized orbital states, showing high electron density concentration, and often correspond to peaks in the partial density of states (PDOS), which is mainly from the Si-p state in the valence band, which is located near the Fermi level.

3.2.2. Partial Density of State (PDOS) Analysis

The partial density of states (PDOS) is computed to analyze the contribution of electronic states in the band structure, as shown in Figures 4, 5, and 6. The two prominent peaks emerge in the valence band, mainly originating from Si-p and O-p states. The highest PDOS peak corresponds to the O-p state, with values of 4.89 eV, 4.94 eV, and 4.88 eV for Ba_3SiO, Sr_3SiO, and Ca_3SiO, respectively. However, the O-p state contributes less to the valence band due to its greater distance from the Fermi level compared to the Si-p state. The second higher peak arises from the Si-p state with PDOS values of 3.22 eV, 3.66 eV, and 2.60 eV for Ba_3SiO, Sr_3SiO, and Ca_3SiO, respectively. These Si-p states are hybridized with smaller Ba-d/Sr-d/Ca-d states, showing high PDOS peaks near the Fermi level as shown in Figures 4(a), 5(a), and 6(a) for Ba_3SiO, Sr_3SiO, and Ca_3SiO, respectively. With respect to the correlation between X cation radius size and the PDOS, the substitution of Sr^{2+} to Ba^{2+} to Ca^{2+}, results in a reduction of the PDOS peak.

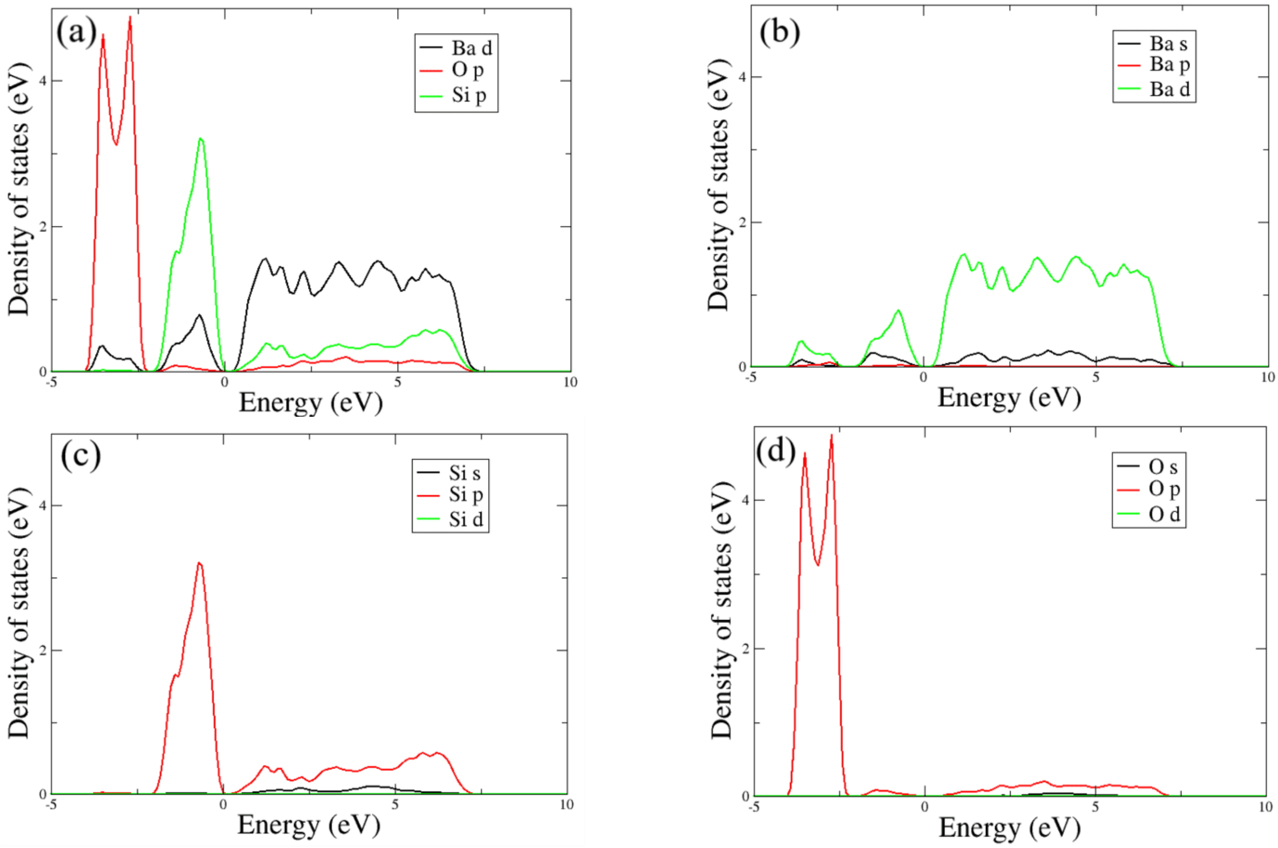

Figure 4. Partial density of state for (a) Ba_3SiO, (b) Ba, (c) Si, and (d) O

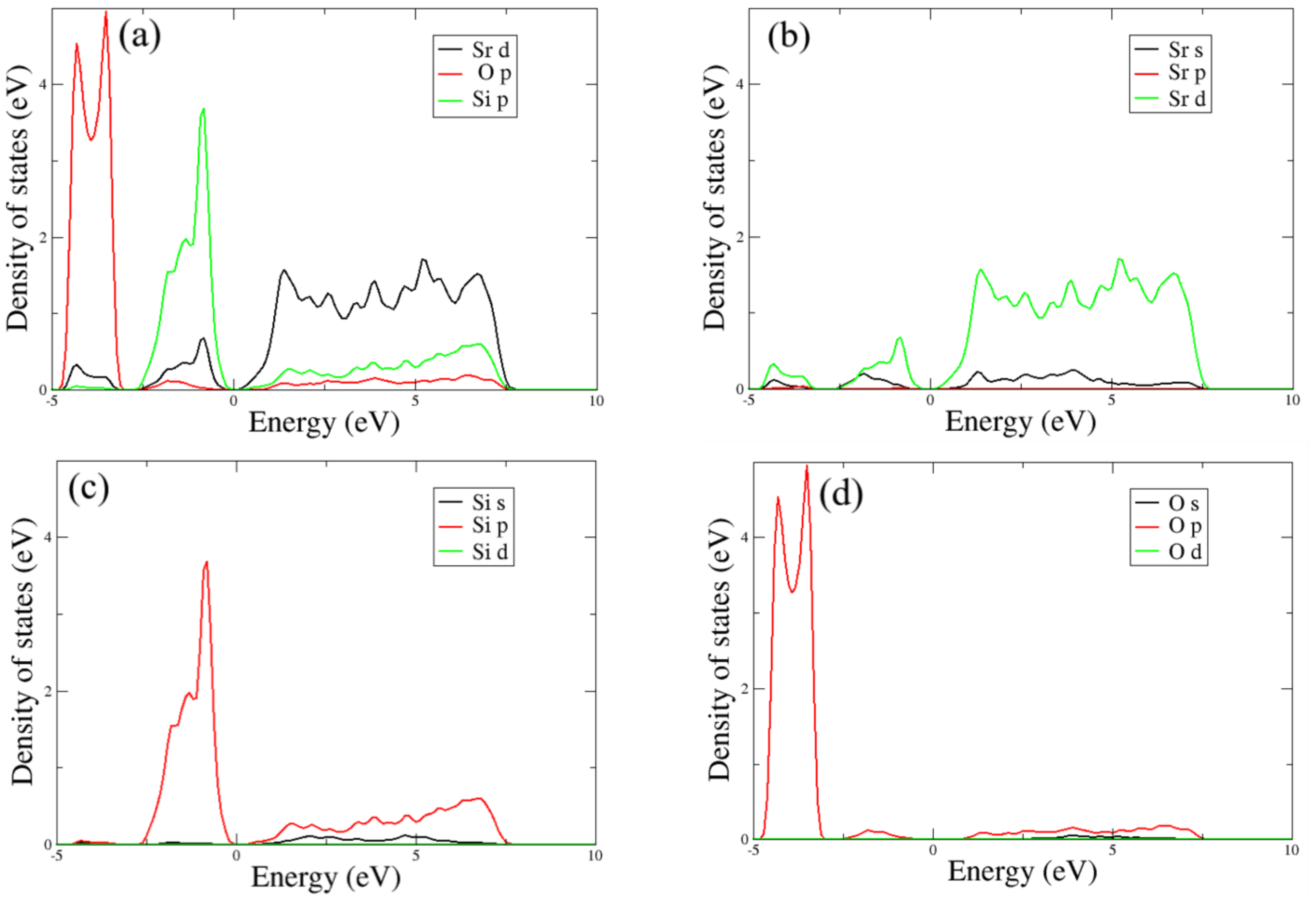

Figure 5. Partial density of state for (a) Sr_3SiO, (b) Sr, (c) Si, and (d) O

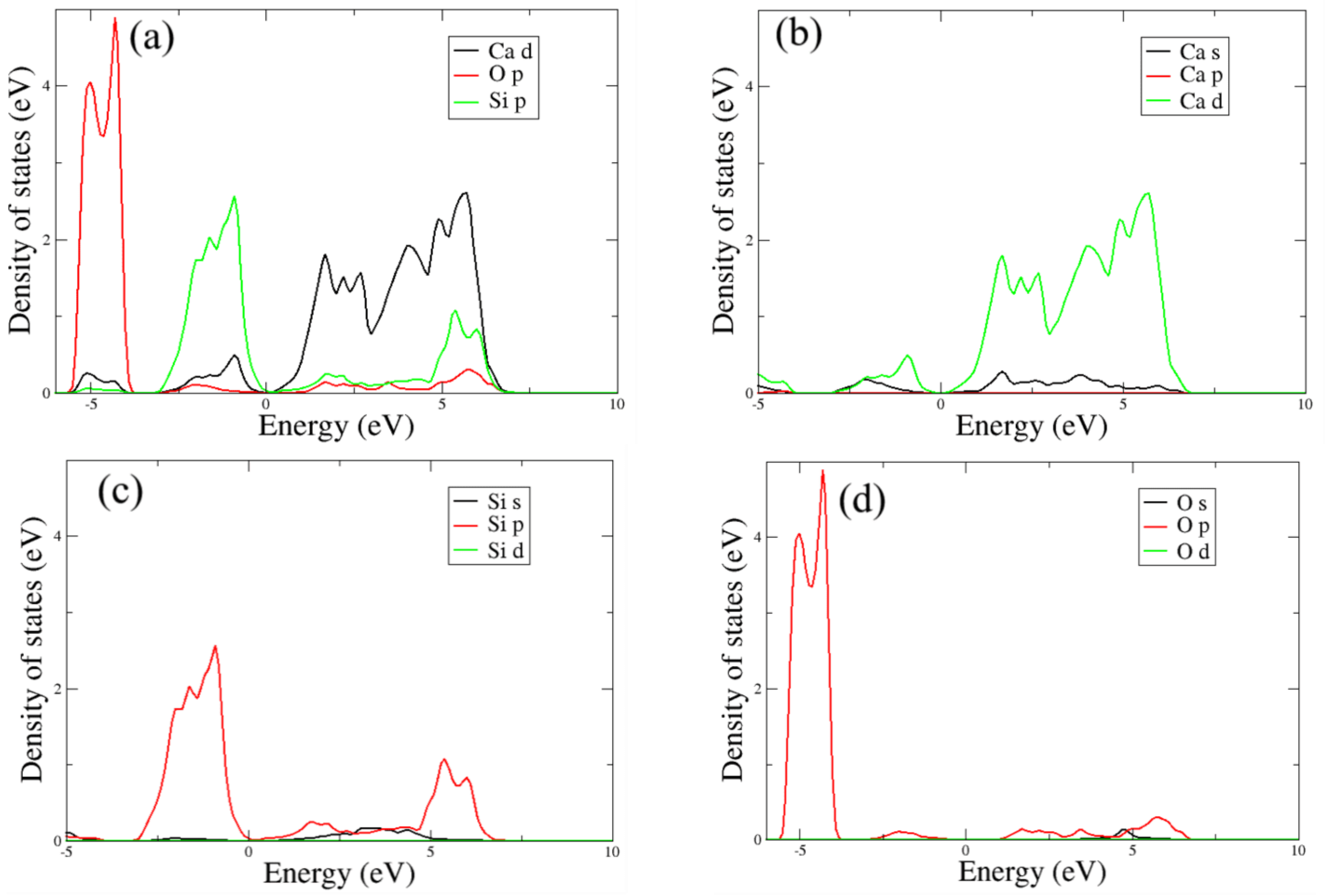

Figure 6. Partial density of state for (a) Ca_3SiO, (b) Ca, (c) Si, and (d) O

The chemical bonding in molecular compounds can be further analyzed through a PDOS plot [27]. The Ba_3SiO, Sr_3SiO, and Ca_3SiO compounds display ionic bonding, as indicated by the differences in PDOS peaks below and above the Fermi level. Above the Fermi level, Ba-d, Sr-d, and Ca-d states dominate, while below the Fermi level, O-p states are predominant. This result is supported by the bond population from Mulliken population analysis, where the bond population values are less than one, confirming the ionic bonding of these compounds. In the valence band, electrons are tightly bound to atoms, leading to high electron density, as observed in the O-p state. In contrast, the electrons are mobile and contribute to electrical conductivity in the conduction band, resulting in lower electron density for Ba-d, Sr-d, and Ca-d states.

In the conduction band, the dominant contribution of electrons comes from Ba-d, Sr-d, and Ca-d states. Figures 4(a), 5(a), and 6(a) also show small electron density contributions from Si-p and O-p states that hybridized with Ba-d, Sr-d, and Ca-d states near the Fermi level. From PDOS analysis, the PDOS peaks are observed at 1.55 eV, 1.71 eV, and 2.59 eV for Ba_3SiO, Sr_3SiO, and Ca_3SiO respectively. Among these peaks, the Ca-d state contributes the highest electron density in the conduction band compared to Ba-d and Sr-d states. Besides, Figures 4(b), 5(b), and 6(b) show that Ba-d, Sr-d, and Ca-d states exhibit lower and broader PDOS peaks compared to the sharper peaks of Si-p and O-p states in the valence band. These low peaks indicate a low electron density concentration that extends across a broad energy range from 0 eV to 7.27 eV for Ba_3SiO, 0 eV to 7.51 eV for Sr_3SiO, and 0 eV to 6.73 eV for Ca_3SiO. The substitution of X cations with different ionic radius sizes from Sr^{2+} to Ba^{2+} to Ca^{2+} causes the reduction of electron density concentration range.

3.3. Thermoelectric Properties

Thermoelectric technology allows the direct conversion of heat energy into electrical energy when the cold part and hot part of semiconducting materials are exposed to temperature gradients, a phenomenon that is known as the Seebeck effect. The efficiency of thermoelectric materials is often governed by the figure of merit (ZT). A high figure of merit indicating better thermoelectric performance of materials. The figure of merit is calculated using Equation (1) as follows [28]:

$$ZT = \frac{S^2\sigma T}{k_{total}} \tag{1}$$

where S^2 is a Seebeck coefficient, σ is electrical conductivity, T is an absolute temperature, and k_{total} is total thermal conductivity. The thermal conductivity comprises two components, which are electronic thermal conductivity (k_{ele}) and lattice thermal conductivity (k_{lat}). The total thermal conductivity can be calculated such that $k_{total} = k_{ele} + k_{1at}$. In this study, the electrical conductivity and total thermal conductivity are calculated with a constant relaxation time of $\tau = 0.8 \times 10^{-14}$ s to determine the value of figure of merit (ZT) [29]. The BoltzTraP code uses a transport tensor to derive the thermoelectric quantities such as the Seebeck coefficient, electrical conductivity, and thermal conductivity. The derived thermoelectric quantities equations is shown below:

$$S_{\alpha\beta}(T,\mu) = \frac{1}{eT\sigma_{\alpha\beta}\Omega}\int \sigma_{\alpha\beta}(\varepsilon)(\varepsilon-\mu)\left[-\frac{\partial f_0(T,\varepsilon,\mu)}{\partial_\varepsilon}\right]d\varepsilon \tag{2}$$

where $S_{\alpha\beta}(T,\mu)$ represents the Seebeck coefficient tensor as a function of temperature and μ is chemical potential, T is an absolute temperature, Ω is a reciprocal space volume, ε is a carrier energy, and σ is an electrical conductivity.

$$\sigma_{\alpha\beta}(T,\mu) = \frac{1}{\Omega}\int \sigma_{\alpha\beta}(\varepsilon)\left[-\frac{\partial f_0(T,\varepsilon,\mu)}{\partial_\varepsilon}\right]d\varepsilon \tag{3}$$

where $\sigma_{\alpha\beta}(T,\mu)$ is the electrical conductivity tensor as a function of temperature and chemical potential, $\sigma_{\alpha\beta}(\varepsilon)$ is energy-dependent conductivity, $(\partial f_\mu\,(T,\varepsilon,\mu))/\,\partial_\varepsilon$ is the derivative of Fermi-Dirac distribution, Ω is the reciprocal space volume, ε is a carrier energy, and μ is the chemical potential.

$$\overset{\circ}{k}_{\alpha\beta}(T,\mu) = \frac{1}{e^2T\Omega}\int \sigma_{\alpha\beta}(\varepsilon)(\varepsilon-\mu)^2\left[-\frac{\partial f_0(T,\varepsilon,\mu)}{\partial_\varepsilon}\right]d\varepsilon \tag{4}$$

where $\overset{\circ}{k}_{\alpha\beta}(T;\mu)$ is an electronic component of thermal conductivity, $(\partial f_\mu\,(T,\varepsilon,\mu))/\,\partial_\varepsilon$ is the derivative of Fermi-Dirac distribution, Ω is the reciprocal space volume, and T is an absolute temperature.

3.3.1. Seebeck Coefficient Analysis

Figure 7 shows the Seebeck S coefficient of Ba_3SiO, Sr_3SiO, and Ca_3SiO compounds as a function of temperature. The Seebeck coefficient curves for these compounds demonstrate a significant decreasing trend with rising temperature from 300 K to 1000 K. At 300 K, the Seebeck coefficient of Ba_3SiO is approximately -4.90×10^{-4} V/K which is lower in magnitude compared to Sr_3SiO with a value of -5.84×10^{-4} V/K. The increase in the Seebeck coefficient of these compounds indicates the generation of voltage as temperature increases. The Ba_3SiO compound also shows negative Seebeck coefficient values from 300 K to 650 K, likewise, Sr_3SiO shows negative S for the

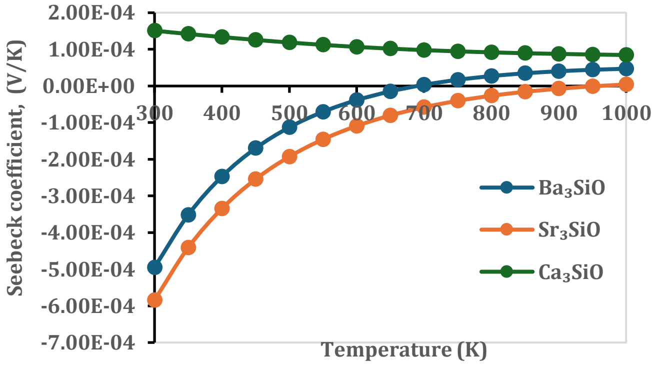

Figure 7. Seebeck coefficient of Ba_3SiO, Sr_3SiO, and Ca_3SiO

temperature range 300 K to 950 K. The negative S implies that the electron is the majority charge carrier. At this temperature range, Ba_3SiO and Sr_3SiO have n-type behavior. From 700 K to 1000 K, Ba_3SiO shows positive S coefficient value, which indicates hole, p, as a majority carrier. Similarly, Sr_3SiO shows a positive S coefficient value at 1000 K.

Meanwhile, Ca_3SiO shows a gradual decreasing trend in Seebeck coefficient with increasing temperature. At 300 K, Ca_3SiO shows a Seebeck coefficient of 1.51×10^{-4} V/K, which decreases to 8.46×10^{-5} V/K at 1000 K. The Ca_3SiO behaves as a p-type from 300 K to 1000 K, as evidenced by its positive Seebeck coefficient. From Seebeck analysis, Sr_3SiO shows the highest Seebeck coefficient in magnitude compared to the Ba_3SiO and Ca_3SiO compounds. The decrease in the Seebeck coefficient at higher temperatures is supposedly due to the effect of phonon scattering [30]. The progressive substitution of the X cation from Ca^{2+} to Ba^{2+} to Sr^{2+} is found to enhance the Seebeck coefficient in the temperature range of 300 K to 1000 K due to the influence of cation size on carrier transport behavior.

3.3.2. Electrical Conductivity Analysis

Figure 8 illustrates the electrical conductivity of Ba_3SiO, Sr_3SiO, and Ca_3SiO compounds. Electrical conductivity refers to the movement of electrical charges within crystal structure [31]. Across all temperatures considered, these compounds exhibit an increasing trend in the electrical conductivity with increasing temperature. For both Ba_3SiO and Sr_3SiO compounds, the electrical conductivity initially increases slowly with the temperature but shows a rapid increase after 800 K. At 300 K, Ba_3SiO has a higher electrical conductivity of 12.1 $(\Omega\cdot m)^{-1}$ compared to Sr_3SiO, which has lower electrical conductivity of 2.08 $(\Omega\cdot m)^{-1}$. Both compounds reach their maximum electrical conductivity at 1000 K, with Ba_3SiO reaching 11359.8 $(\Omega\cdot m)^{-1}$ and Sr_3SiO reaching 5604.4 $(\Omega\cdot m)^{-1}$.

On the other hand, Ca_3SiO shows a rapidly increasing trend in electrical conductivity from 300 K to 1000 K. At 300 K, Ca_3SiO exhibits the electrical conductivity value of 5610.2 $(\Omega\cdot m)^{-1}$ and it reaches a maximum electrical conductivity of 41378.7 $(\Omega\cdot m)^{-1}$ at 1000 K. From electrical conductivity analysis, Ca_3SiO demonstrates the highest electrical conductivity from 300 K to 1000 K compared to the Ba_3SiO and Sr_3SiO compounds. The higher electrical conductivity of Ca_3SiO compared to Ba_3SiO and Sr_3SiO is mainly due to the lower Seebeck coefficient, as both of these parameters are inversely proportional. The substitution of X cations from Sr^{2+} to Ba^{2+} to Ca^{2+}, results in higher electrical conductivity from 300 K to 1000 K.

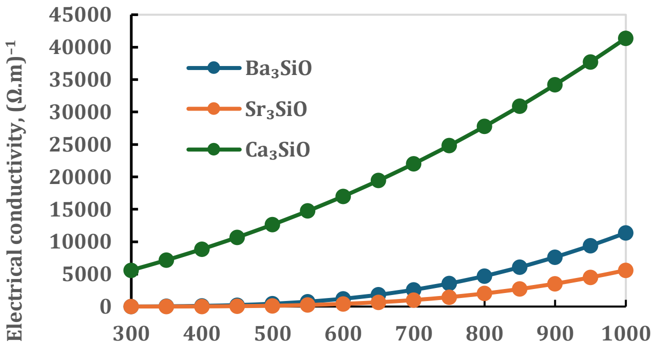

Figure 8. Electrical conductivity of Ba_3SiO, Sr_3SiO, and Ca_3SiO

3.3.3. Thermal Conductivity Analysis

The calculated electronic thermal conductivity and lattice thermal conductivity of the Ba_3SiO, Sr_3SiO, and Ca_3SiO compounds are shown in Figures 9(a) and 9(b). For electronic thermal conductivity, these compounds exhibit a higher value from 300 K to 1000 K. At 300 K, the electronic thermal conductivity of Ba_3SiO, Sr_3SiO, and Ca_3SiO is 2.45×10^{-3} W/mK, 5.42×10^{-4} W/mK, and 0.13 W/mK, while these compounds reached the maximum point with values of 2.07 W/mK, 1.26 W/mK, and 3.88 W/mK, respectively, at 1000 K.

As the temperature rises, the number of excited charge carriers increases, thereby strengthening the electronic thermal conductivity due to the increased mobility of free electrons in the crystal [32]. Besides, the higher electrical conductivity is also related to the higher electronic thermal conductivity. This trend necessarily follows the Wiedemann-Franz law, which states that the electronic thermal conductivity (k_{ele}) is directly proportional to electrical conductivity (σ) with the formula $k_{ele} = L\sigma T$ [33]. Furthermore, the electron transitions between the valence band and conduction band take place with minimal changes in momentum for a direct band gap. This indicates that electrons transition from the valence band to the conduction band with minimal scattering, facilitating efficient electron transport. As a result, material with direct band gaps exhibits higher thermal conductivity, as heat can be effectively delivered by the electrons [34].

In terms of lattice thermal conductivity, all three compounds show a decreasing trend as temperature increases. This behavior is common for various materials because the heat transfer is impeded by increased phonon scattering at high temperatures. Ca_3SiO shows the highest lattice thermal conductivity from 300 K to 1000 K, with the values of 1.39 W/mK to 0.46 W/mK, respectively, and Ba_3SiO demonstrates moderate lattice thermal conductivity values of 0.91 W/mK at 300 K to 0.28 W/mK at 1000 K. Meanwhile, Sr_3SiO displays the lowest lattice thermal conductivity, starting at about 0.22 W/mK at 300 K and decreasing to 0.07 W/mK at 1000 K.

Figure 9(c) presents the calculated total thermal conductivity of Ba_3SiO, Sr_3SiO, and Ca_3SiO compounds as a function of temperature. This plot shows that these compounds display a gradual improvement followed by a rapid rise until reaching a maximum point at 1000 K. At 300 K, the total thermal conductivity values of Ba_3SiO, Sr_3SiO, and Ca_3SiO are 0.91 W/mK, 0.22 W/mK, and 1.53 W/mK, respectively. At 1000 K, the total thermal conductivity value increased to 2.35 W/mK, 1.34 W/mK, and 4.35 W/mK for Ba_3SiO, Sr_3SiO, and Ca_3SiO, respectively. From thermal conductivity analysis, the higher total thermal conductivity is related to the higher lattice thermal conductivity. From thermal conductivity analysis, Ca_3SiO shows the highest total thermal conductivity because the smaller ionic radius of Ca^{+2} can enhance more phonon transport, which assists better heat transfer in the crystal structure efficiently compared to the ionic radii of Sr^{2+} and Ba^{2+}. Therefore, the substitution of different X cations from Sr^{2+} to Ba^{2+} to Ca^{2+}, results in an increase in the total thermal conductivity from 300 K to 1000 K.

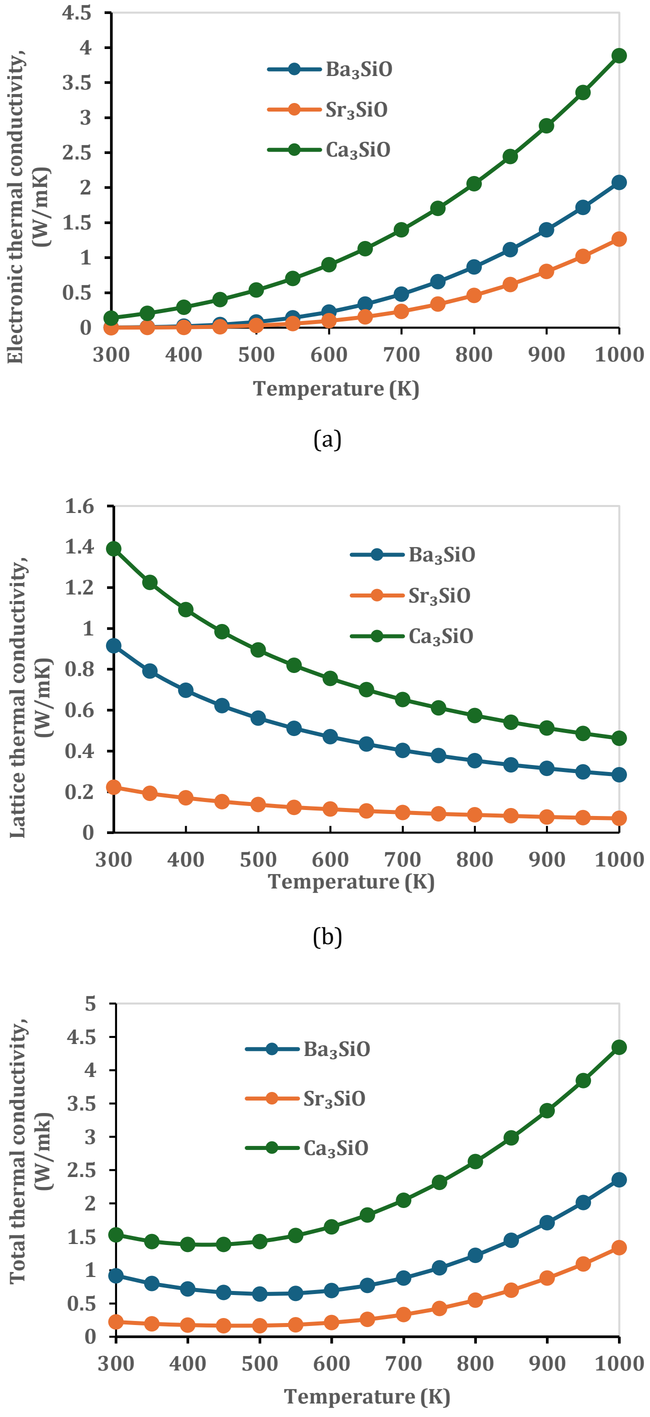

(a)

(b)

(c)

Figure 9. The calculated (a) electronic thermal conductivity, (b) lattice thermal conductivity and (c) total thermal conductivity of Ba_3SiO, Sr_3SiO, and Ca_3SiO

3.3.4. Figure of Merit Analysis

The figure of merit (ZT) can be calculated once all required transport properties, including the Seebeck coefficient, electrical conductivity, and total thermal conductivity, are determined. Figure 10 depicts the calculated figure of merit for Ba_3SiO, Sr_3SiO, and Ca_3SiO compounds. For Ba_3SiO, the ZT curve initially increases from 300 K to 450 K with a value of 9.66×10^{-4} to 4.5×10^{-3}, respectively. After reaching a peak at 450 K, the ZT curve experiences a decline from 500 K to 700 K, approximately 4.34×10^{-3} to 2.26×10^{-5}, respectively. However, above 750 K, the ZT curve rises sharply until approaching a value of 7.36×10^{-4} to 1.06×10^{-2} as temperature increases from 750 K to 1000 K, respectively.

For Sr_3SiO, the ZT curve exhibits a significant increase from 300 K to 500 K with values of 9.59×10^{-4} to 1.45×10^{-2}, respectively, and reaches the maximum peak at 550 K with a value of 1.57×10^{-2}. However, from 600 K to 900 K, the ZT curve declines with a value of 1.40×10^{-2} to 2.00×10^{-4}, respectively. From 950 K to 1000 K, the curve decreased from 3.28×10^{-6} to 7.06×10^{-5}, respectively.

In contrast to Ba_3SiO and Sr_3SiO, the ZT curve of Ca_3SiO shows a sharp increase initially and then a slight decline until reaching a point at 1000 K. From 300 K to 600 K, the ZT rises sharply with the value from 2.50×10^{-2} to 7.03×10^{-2}, respectively. However, from 650 to 1000 K, the ZT curve declines with the value from 7.18×10^{-2} to 6.81×10^{-2}, respectively. From figure of merit analysis, these compounds exhibit poor thermoelectric performance as reflected by their low ZT value from 300 K to 1000 K. The lower ZT values are primarily related to their higher total thermal conductivity, which shows the decreasing of efficiency of thermoelectric conversion from heat energy to electrical energy. The substitution of the X cation from Sr^{2+} to Ba^{2+} to Ca^{2+}, results in a higher figure of merit at 300 K, while at 1000 K, the substitution of the X cation for Ca^{2+} also shows the highest ZT compared to Ba^{2+} and Sr^{2+}.

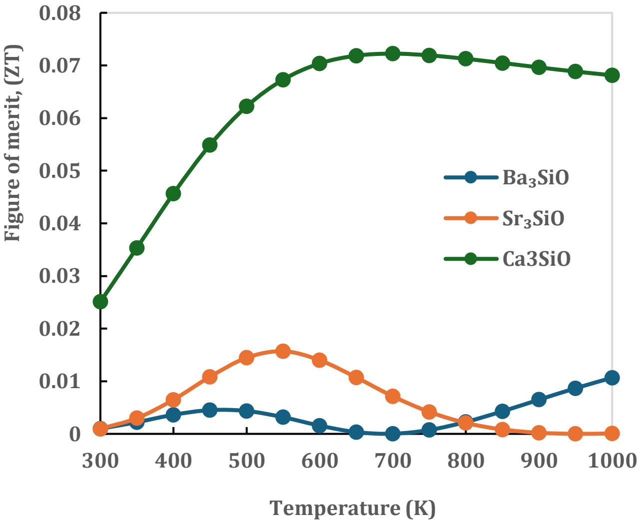

Figure 10. Figure of merit for Ba_3SiO, Sr_3SiO, and Ca_3SiO

3.4. Optical Properties

The dielectric function plays an important role in determining the optical properties of X_3SiO (X = Ba, Sr, Ca), including energy loss function, reflection coefficient, absorption coefficient, optical conductivity, and refractive index. It can be expressed using the following Equation (5) [35–36]:

$$\varepsilon(\omega) = \varepsilon_1(\omega) + i\varepsilon_2(\omega) \tag{5}$$

where $\varepsilon_1(\omega)$ is a real part and $\varepsilon_2(\omega)$ is an imaginary part of the dielectric function. The real part of the dielectric function is calculated based on the Kramers-Kronig equation which is given by Equation (6):

$$\varepsilon_1(\omega) = 1 + \frac{2}{\pi} P \int_0^\infty \frac{\varepsilon_2(\omega')\omega' d\omega'}{(\omega')^2 - (\omega)^2} \tag{6}$$

Here, P represents the Cauchy principle value of the integral. The imaginary part $\varepsilon_2(\omega)$of the dielectric function is determined from the momentum matrix elements in between occupied and unoccupied orbitals and is derived using the following Equation (7):

$$\varepsilon_2 = (\omega) = \frac{Ve^2}{2\pi\hbar m^2\omega^2} \int d^3k \sum |\langle\psi_c|p|\psi_v\rangle|^2 \, \delta(E_c - E_v - \hbar\omega) \tag{7}$$

In this equation, p denotes the momentum operator, ψ_c to ψ_v are the point to the conduction and valence bands, $\hbar$ is the reduced Planck constant and ωis the frequency of the incident ray.

3.4.1. Dielectric Function Analysis

Figure 11 illustrates the calculated dielectric function of X_3SiO (X= Ba, Sr, Ca) compounds, which comprises of both real part $\varepsilon_1(\omega)$ and imaginary part $\varepsilon_2(\omega)$. The real part at zero frequency limit, $\varepsilon_1(0)$ is also known as static dielectric function, indicates the ability of material to become electrically depolarized when subjected to an external electrical field [37]. The static dielectric functions were determined to be approximately 16.94 for Ba_3SiO, 14.12 for Sr_3SiO, and 50.08 for Ca_3SiO.

Above zero-frequency limit, the maximum peaks in the $\varepsilon_1(\omega)$ were observed at 1.03 eV (24.06) for Ba_3SiO, at 0.66 eV (18.12) for Sr_3SiO, and at 0.10 eV (80.46) for Ca_3SiO. These peaks indicate significant absorption of light energy within the infrared (IR) region for Ba_3SiO, Sr_3SiO, and Ca_3SiO, showing that these compounds have strong IR absorption. Among these compounds, Ca_3SiO exhibits the highest dielectric function due to its smaller band gap, leading to higher light absorption capability compared to Ba_3SiO and Sr_3SiO compounds. With respect to X cation substitution, the replacement of Ba^{2+} to Sr^{2+} to Ca^{2+} induces an increase in dielectric function. This reflecting the influence of cation size on the band gap of these compounds.

Furthermore, the positive values of $\varepsilon_1(\omega)$ indicate that these materials exhibit dielectric behavior. However, when $\varepsilon_1(\omega)$ becomes negative, the materials change from dielectric behavior to metal-like behavior. The $\varepsilon_1(\omega)$ curves show that all three compounds exhibit negative values in the visible and ultraviolet regions, suggesting their ability to reflect the electromagnetic wave. Particularly, Ba_3SiO displays the negative values from 2.23 eV (−1.43) to 3.15 eV (−1.90) and at 7.60 eV (−1.20). Meanwhile, Ca_3SiO shows the negative value from 4.40 eV (−3.69) to 7.34 eV (−2.12), and Sr_3SiO displays the negative value from 3.07 eV (−4.12) to 3.85 eV (−3.44). When $\varepsilon_1(\omega)$ is less than zero, it implies that the electromagnetic wave cannot propagate into the solid materials in the visible and ultraviolet region, thus validate their reflective characteristics in these regions.

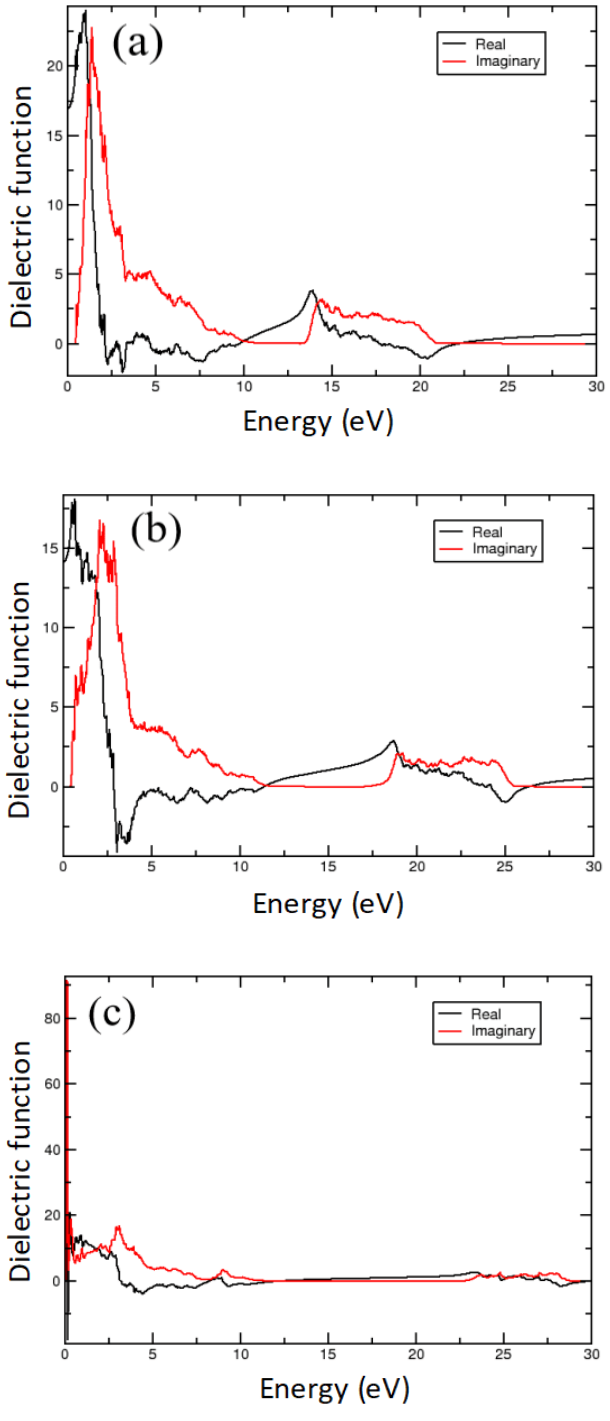

Figure 11. Dielectric function of (a) Ba_3SiO, (b) Sr_3SiO, and (c) Ca_3SiO

The calculated imaginary part of dielectric function, $\varepsilon_2(\omega)$, is represented by the red curve in Figure 11. The $\varepsilon_2(\omega)$ is define how the materials absorb the electromagnetic wave. The $\varepsilon_2(\omega)$ curve shows the optical gap at 0.48 eV, 0.46 eV, and 0.10 eV for Ba_3SiO, Sr_3SiO, and Ca_3SiO compounds, respectively. These optical gaps verify the conductivity of these compounds as a semiconductor material. The increases and decreases curve in $\varepsilon_2(\omega)$ show that the band transition takes place in certain region. The main peaks of $\varepsilon_2(\omega)$ determined at 1.80 eV for Ba_3SiO, 2.08 eV for Sr_3SiO, and 0.33 eV for Ca_3SiO. These peaks indicate the intraband transition that relates with the energy of absorbed photons [38]. At these peaks also, the interband transitions occur from the valence band to the conduction band along direction of Γ–Z k-points for Ba_3SiO, Sr_3SiO, and Ca_3SiO compounds. These transitions involve from Si-p state to Ba-d in Ba_3SiO, Si-p state to Sr-d state in Sr_3SiO, and Si-p state to Ca-d state in Ca_3SiO.

3.4.2. Energy Loss Function Analysis

Figure 12 presents the calculated energy loss function of X_3SiO (X = Ba, Sr, Ca) compounds. In the ultraviolet region (>20 eV), the Ba_3SiO, Sr_3SiO, and Ca_3SiO compounds exhibit sharp and prominent peaks at 22.23 eV (240.24), at 26.38 eV (54.94), and at 29.86 eV (444.37), respectively. These higher peaks of the energy loss function result from volume plasmon oscillations, representing the collective charge oscillations and indicating the rapid reduction in reflectance [39], while a sharp peak of the energy loss function correspond to the absorption of plasmon energy. The primary cause of energy loss in these compounds is the ambient ionization and oscillation of electrical dipoles [40]. In addition, the lower peaks were also observed at 11.36 eV (9.57) for Sr_3SiO and at 12.14 eV (26.06) for Ca_3SiO, which are due to surface plasmon oscillation. In the infrared to visible region, the energy loss of these compounds shows a nearly flat region from 0 eV to 10 eV, indicating a minimum energy loss. These results show that these compounds experience limited energy dissipation in this region, which makes them transparent. For X cation substitution effects on the energy loss function, the replacement of Sr^{2+} to Ba^{2+} to Ca^{2+} shows an increasing trend in the energy loss function.

3.4.3. Reflection Coefficient Analysis

Figure 13 illustrates the calculated reflection coefficient of X_3SiO (X = Ba, Sr, Ca) compounds. At the zero-frequency limit, the static optical reflection was determined to be approximately 37.11% for Ba_3SiO, 33.62% for Sr_3SiO, and 56.62% for Ca_3SiO. In the infrared to visible region, the reflection curves start at 0 eV and increase to their peaks at 1.38 eV with 50.88% reflection for Ba_3SiO, at 2.96 eV with 53.31% reflection for Sr_3SiO, and at 0.17 eV with 73.01% reflection for Ca_3SiO.

The highest reflection peaks of X_3SiO (X = Ba, Sr, Ca) compounds were observed in the high ultraviolet region (>20 eV). Specifically, Ba_3SiO shows a peak at 20.54 eV with 68.89% reflection, Sr_3SiO, with 94.60% reflection at 25.61 eV and Ca_3SiO reaches 99.88% reflection at 29.63 eV. These highest peaks that are above 21.30% indicate that these compounds are highly reflective in this region, which suggests their potential for ultraviolet shield application. Moreover, these compounds also exhibit low reflection (high transparency) in the ultraviolet region, particularly, Ba_3SiO shows a low reflection from 11 eV to 12.5 eV, Sr_3SiO around 15 eV and Ca_3SiO between 15 eV and 20 eV. For X cation substitution, the replacement of Ba^{2+} to Sr^{2+} to Ca^{2+} displays an increasing trend in reflection coefficient.

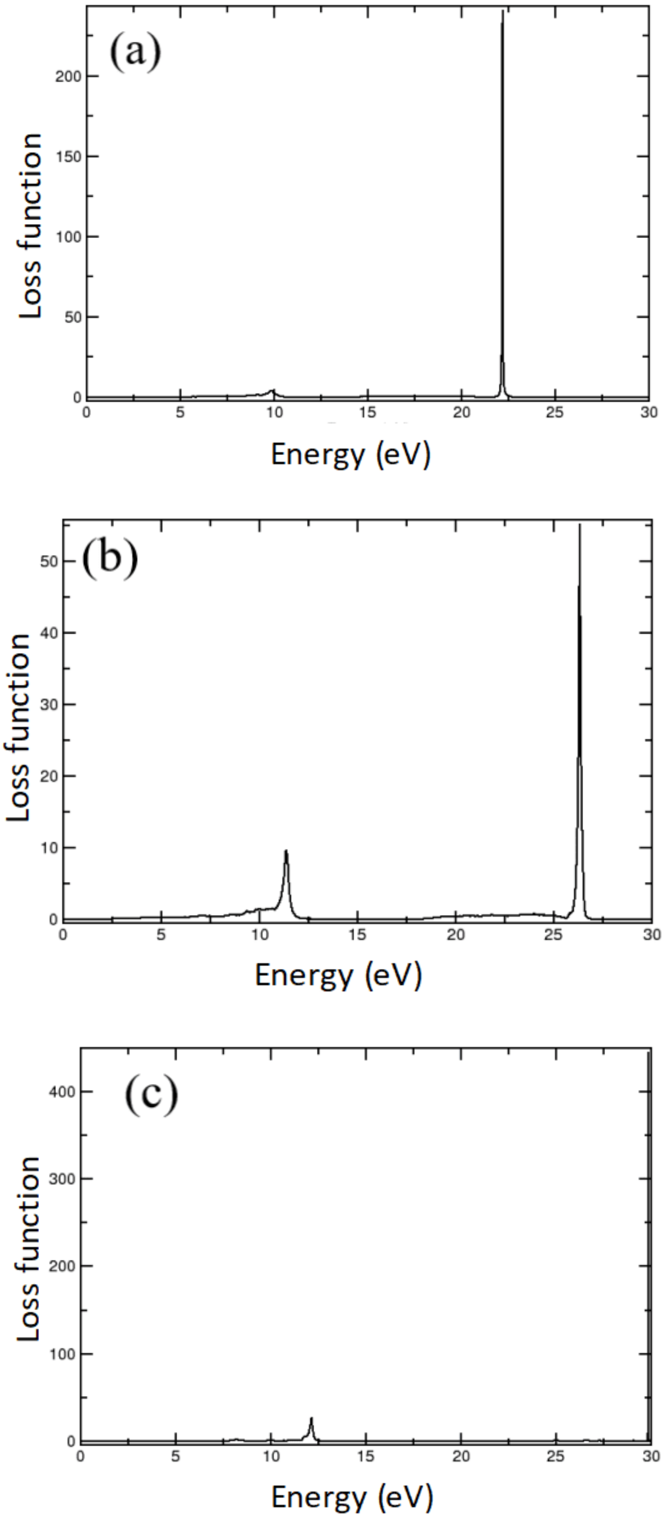

Figure 12. Energy loss function of (a) Ba_3SiO, (b) Sr_3SiO, and (c) Ca_3SiO

3.4.4. Absorption Coefficient Analysis

A high absorption coefficient in solid materials is associated with efficient electron transport from the valence band to the conduction band, resulting in better optical performance [41]. Figure 14 displays the calculated absorption coefficient of X_3SiO (X = Ba, Sr, Ca) compounds. The optical gaps were determined at 0.47 eV, 0.46 eV, and 0.10 eV for Ba_3SiO, Sr_3SiO, and Ca_3SiO respectively, which are validate the semiconductor nature of these compounds. The absorption coefficient of these compounds displays a maximum peak in the visible region at 3.07 eV with an absorption of 6.90×10^7 m^{-1} for Ba_3SiO, at 3.07 eV with an absorption of 8.74×10^7 m^{-1} for Sr_3SiO, and at 3.12 eV with an absorption of 8.87×10^7 m^{-1} for Ca_3SiO. These peaks highlight that these compounds are effective absorber of electromagnetic wave in the visible region.

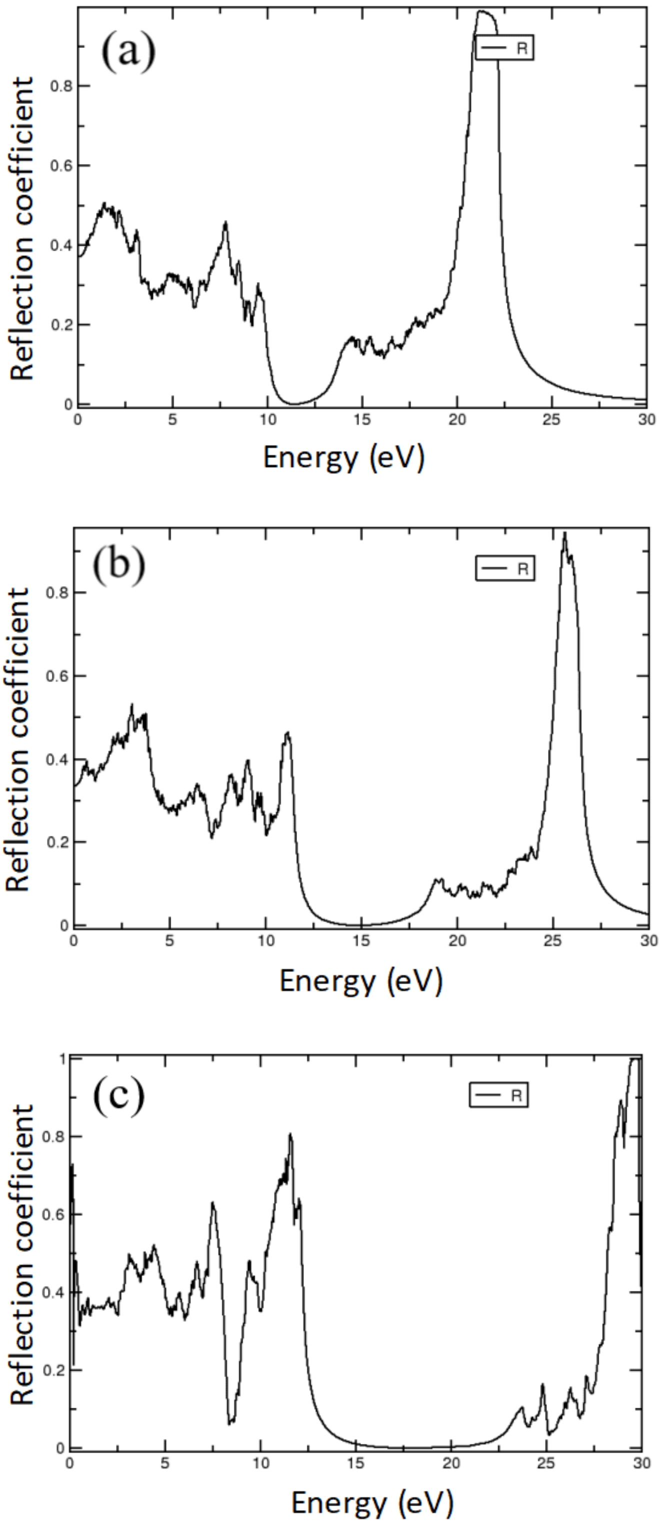

Figure 13. Reflection coefficient of (a) Ba_3SiO, (b) Sr_3SiO, and (c) Ca_3SiO

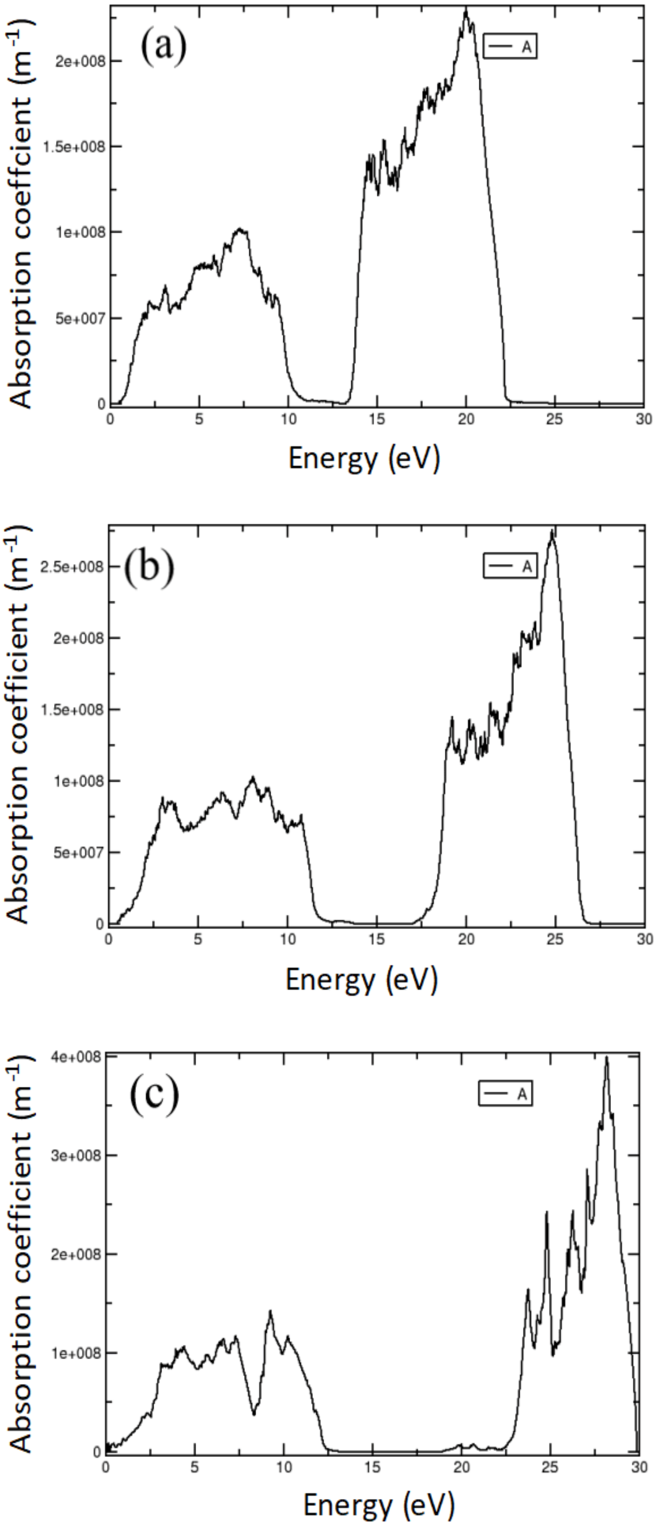

Figure 14. Absorption coefficient of (a) Ba_3SiO, (b) Sr_3SiO, and (c) Ca_3SiO

From absorption coefficient analysis, Ba_3SiO, Sr_3SiO, and Ca_3SiO shows a high absorption peaks in ultraviolet region. These peaks were determined approximately at 7.30 eV with 1.02×10^8 m^{-1} absorption for Ba_3SiO, at 8.10 eV with 1.03×10^8 m^{-1} absorption for Sr_3SiO, and at 9.26 eV with 1.43×10^8 m^{-1} absorption for Ca_3SiO. In high ultraviolet region (above 18 eV), the absorption peaks reach their maximum values at 20.02 eV with an absorption of 2.30×10^8 m^{-1} for Ba_3SiO, at 24.84 eV with an absorption of 2.75×10^8 m^{-1} for Sr_3SiO, and at 28.15 eV with an absorption of 3.98×10^8 m^{-1} for Ca_3SiO. For correlation of X cation substitution, the replacement of Ba^{2+} to Sr^{2+} to Ca^{2+} shows an increases trend in absorption coefficient. The results indicate the potential of Ba_3SiO, Sr_3SiO, and Ca_3SiO for ultraviolet detector. According to Song *et al.*, a high absorption coefficient of materials is also advantageous for efficient light absorption in thin-film solar cell devices [42]. Therefore, these compounds also probable candidates for thin-film solar cell devices due to their high absorption coefficient.

3.4.5. Optical Conductivity Analysis

Optical conductivity describes how material react to an electrical field when exposed to electromagnetic wave. Figure 15 shows the calculated optical conductivity of X_3SiO (X = Ba, Sr, Ca) compounds. The real and imaginary parts of optical conductivity for these compounds indicate that the curves do not begin at 0 eV, which shows that these compounds are semiconductor materials. The maximum peaks for the real part in the visible region appeared at 1.79 eV with a conductivity of 438059 $S{\cdot}m^{-1}$ for Ba_3SiO, at 2.85 eV with a conductivity of 590312 $S{\cdot}m^{-1}$ for Sr_3SiO, and at 3.15 eV with a conductivity of 694493 $S{\cdot}m^{-1}$ for Ca_3SiO. These peaks are attributed to the interband transitions along high symmetry k-points in the electronic band structures. The energy range from 0 eV to 3.5 eV is corresponds to interband transitions involving the Si-p state in the valence band to Ba-d, Sr-d, and Ca-d states in the conduction band at Γ–Z k-points.

In ultraviolet region, the real part of optical conductivity for these compounds shows the highest peaks at 14.45 eV with a conductivity of 622978 $S{\cdot}m^{-1}$ for Ba_3SiO, at 22.65 eV with a conductivity of 578056 $S{\cdot}m^{-1}$ for Sr_3SiO, and at 27.07 eV with a conductivity of 975989 $S{\cdot}m^{-1}$ for Ca_3SiO. For the effect of X cation substitution, the replacement of Ba^{2+} to Sr^{2+} to Ca^{2+} shows an increases trend in optical conductivity. Among these compounds, Ca_3SiO exhibits the highest optical conductivity, implying that the highest absorption occurs in this region. These results show that all three compounds exhibit higher optical conductivity, making these compounds suitable for optoelectronic devices in visible and ultraviolet regions.

3.4.6. Refractive Index Analysis

The refractive index consists of both a real part, denoted as n(ω), which illustrates the propagation of photon wave through a solid material in different media, and an imaginary part, denoted as k(ω), representing the photon wave absorption behavior within the material. Figure 16 shows the calculated refractive index of X_3SiO (X = Ba, Sr, Ca) compounds. The refractive index (n) is essential for studying solid material to understand the electromagnetic wave behavior as it travels through the materials. In literature, Islam *et al.* reported that a high refractive index (n) is a key indicator for solid material intended for using in optoelectronic device applications [43]. This is because a high refractive index is important to bend and slow down more the light spectrum in fabricating the optical devices.

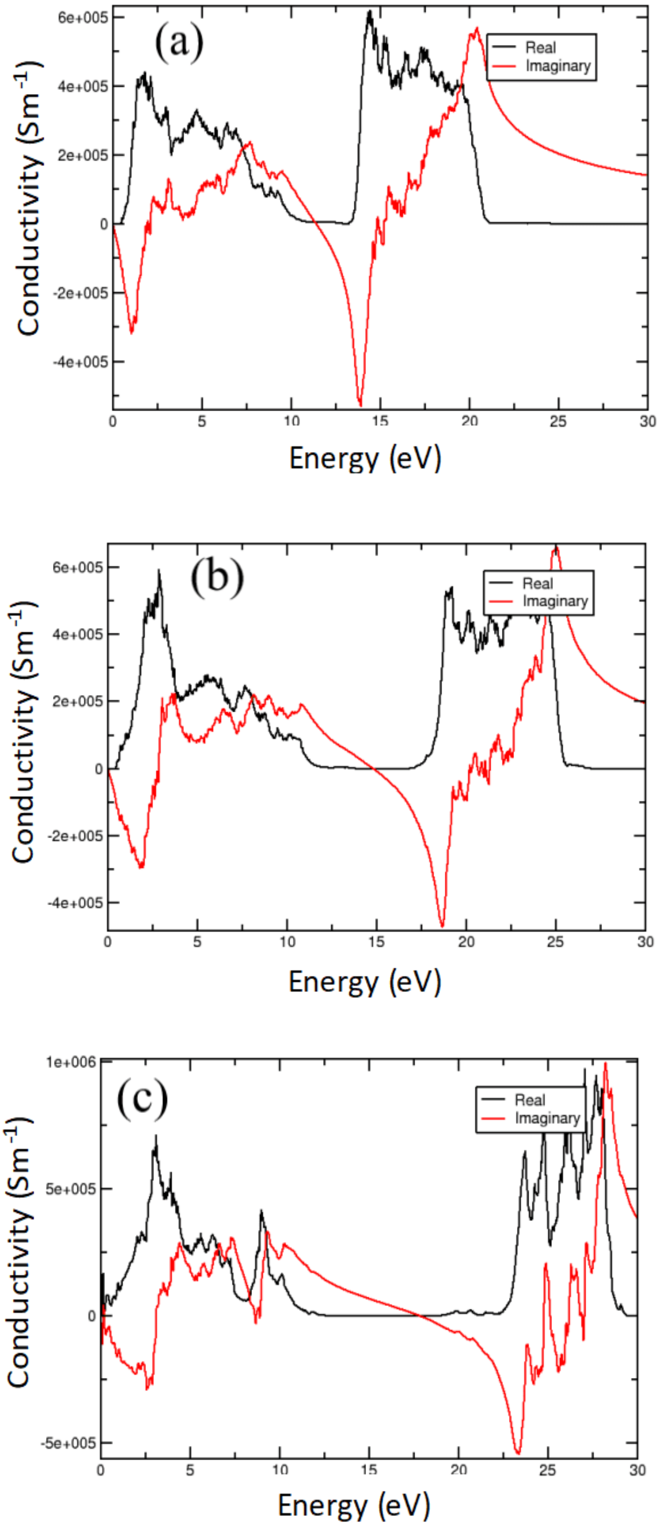

Figure 15. Optical conductivity of (a) Ba_3SiO, (b) Sr_3SiO, and (c) Ca_3SiO

The static refractive index $n(0)$ is observed at 4.11 for Ba_3SiO, 3.76 for Sr_3SiO, and 7.07 for Ca_3SiO. On the other hand, the maximum peaks of $n(\omega)$ for these compounds appeared in the visible region. In particular, Ca_3SiO displays the highest peak at 2.89 eV with refractive index value of 3.57 and surpassing the peaks of Ba_3SiO and Sr_3SiO at 2.11 eV (2.88) and 2.84 eV (2.90), respectively. These peaks occurred in the visible region are attributed to the intraband transitions. In this region also, these compounds display a high transparency to electromagnetic wave which allowing the higher number of light energy photons to traverse through solid material. From this analysis, these peaks indicate that these compounds possess refractive properties in the visible region. The replacement of Ba^{2+} to Sr^{2+} to Ca^{2+} for X cation effect show an increases trend in refractive index.

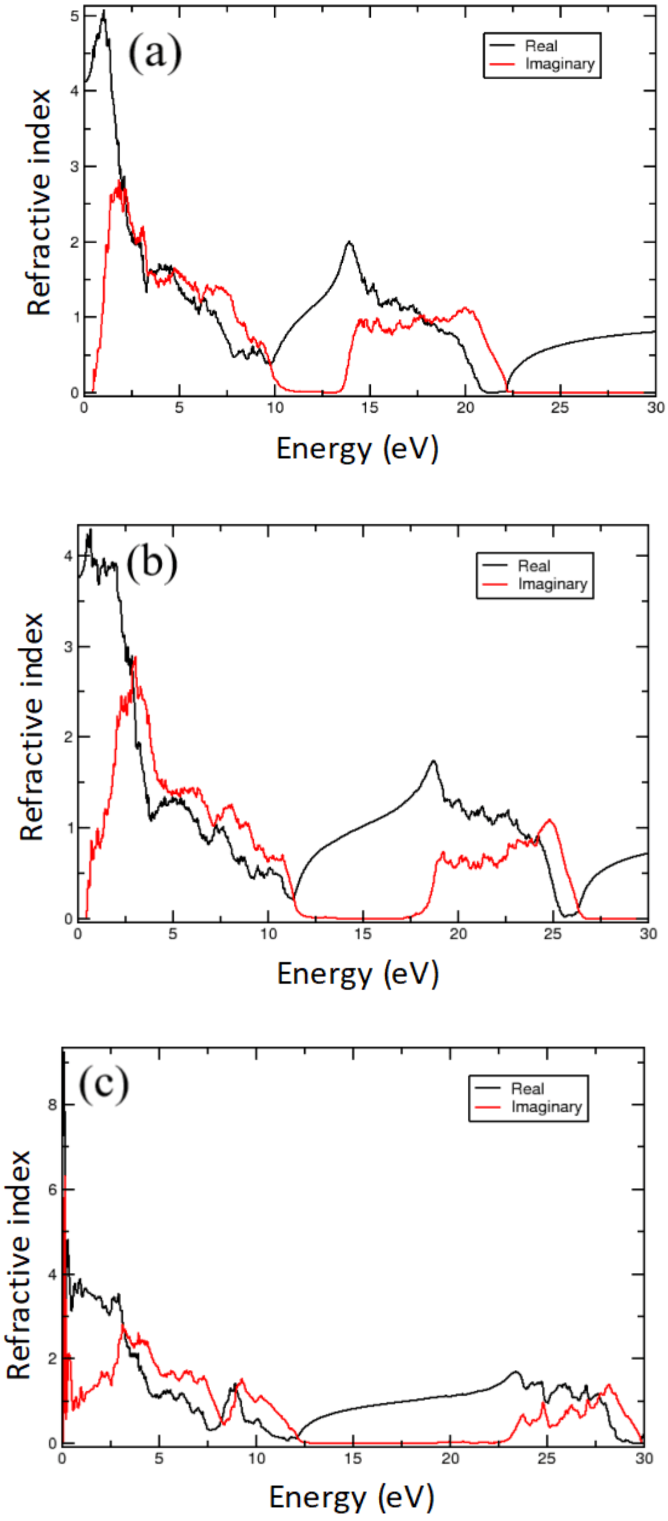

Figure 16. Refractive index of
(a) Ba_3SiO, (b) Sr_3SiO, and (c) Ca_3SiO

The imaginary part of the refractive index, also referred as the extinction coefficient $k(\omega)$, measures the reduction in incident light as it propagates through solid material. For Ba_3SiO, Sr_3SiO, and Ca_3SiO compounds, the extinction coefficient started at 0 eV and increases until reaching the maximum values in the infrared to visible regions. The maximum peaks were determined at 1.83 eV (2.82) for Ba_3SiO, at 3.04 eV (2.89) for Sr_3SiO, and at 0.16 eV (6.29) for Ca_3SiO, respectively. These peaks represent the points where electromagnetic wave experiences the most significant reduction as it passes through the materials. According to Hong *et al.*, a high refractive index of material with $n \geq 1.7$ indicate that the material has a considerable potential as candidates for photonic and optoelectronic devices [44].

4. CONCLUSION

We conducted a first-principles study on anti-perovskite compounds to investigate the structural, electronic, thermoelectric, and optical properties of X_3SiO (X = Ba, Sr, Ca) using generalized gradient approximation with the Perdew-Burke-Enzzerhof (GGA-PBE) functional within the density functional theory method. The band structure analysis shows that the band gaps were determined to be 0.44 eV, 0.43 eV, and 0.11 eV for Ba_3SiO, Sr_3SiO, and Ca_3SiO, respectively. These compounds show a narrow band gap under 0.5 eV, which is probable for optical applications. All calculated band structures of these compounds were found to have semiconducting behavior with direct band gaps at k-points. The calculated lattice parameters and band structures of anti-perovskite X_3SiO (X = Ba, Sr, Ca) were in good agreement with previous studies. Based on the Pugh's ratio, these compounds were classified as brittle materials with the Pugh's ratio value less than 1.75. In addition, these compounds also exhibited high Young's modulus, indicating considerable stiffness and the ability to withstand deformation under compression and tension forces. However, their low bulk modulus shows that these materials can be compressed under certain high, uniform pressures. Furthermore, the stiffness and hardness of the X cation increase in trend in order from Ba^{2+} to Sr^{2+} to Ca^{2+}. For thermoelectric property analysis, the Seebeck coefficient, electrical conductivity, thermal conductivity, and figure of merit were calculated using the Boltzmann transport equation (BTE) in BoltzTrap code. The Seebeck coefficient analysis shows that Ca_3SiO is a p-type compound, while Ba_3SiO shows an n-type compound in the temperature range of 300 to 650 K and a p-type compound above 650 K. Sr_3SiO also shows an n-type compound for the temperature range of 300 K to 900 K and a p-type compound at 1000 K. Ca_3SiO has the highest conductivity values from 300 K to 1000 K compared to Ba_3SiO and Sr_3SiO. For thermal conductivity analysis, Ca_3SiO also shows the highest total thermal conductivity values from 300 K to 1000 K compared to Ba_3SiO and Sr_3SiO. For figure of merit, Ca_3SiO shows the highest values at 300 K and at 1000 K compared to Ba_3SiO and Sr_3SiO. For optical property analysis, dielectric function, absorption coefficient, reflection coefficient, optical conductivity, energy loss function, and refractive index were analyzed. The maximum peaks in the high ultra-violet light energy range (>20 eV) suggest that these compounds are excellent reflectors in this range. Hence, anti-perovskite X_3SiO (X=Ba, Sr, Ca) are suitable candidates for ultraviolet shield applications. Furthermore, the Ca_3SiO compound exhibited high optical properties compared to Ba_3SiO and Sr_3SiO. It showed a high dielectric function of 80.46 at 0.10 eV in the infrared region, an absorption coefficient of 3.98×10^8 m^{-1} at 28.15 eV in the high ultraviolet region, and a refractive index of 3.57 at 2.89 eV in the visible region. Among these compounds, Ca_3SiO is a potential material for thermoelectric and optical applications compared to Ba_3SiO and Sr_3SiO.

ACKNOWLEDGMENTS

This work was funded by the Ministry of Higher Education (MoHE) through the Fundamental Research Grant Scheme (FRGS/1/2022/STG05/UNIMAP/01/1). We also express our gratitude to the Malaysia government for supporting this work through the self-funded research grant. MyBrain15 program and research grant, L00022 provided by the Ministry of Science, Technology, and Innovation (MOSTI).

REFERENCES

[1] S. v. Krivovichev, “Minerals with antiperovskite structure: a review,” *Zeitschrift für Kristallographie - Crystalline Materials*, vol. 223, no. 1–2, pp. 109–113, 2008, doi: 10.1524/zkri.2008.0008.

[2] Y. Sun *et al.*, “Neutron Diffraction Study of Unusual Phase Separation in the Antiperovskite Nitride Mn_3ZnN,” *Inorganic Chemistry*, vol. 51, no. 13, pp. 7232–7236, 2012, doi: 10.1021/ic300978x.

[3] M. Massetti *et al.*, “Unconventional Thermoelectric Materials for Energy Harvesting and Sensing Applications,” *Chemical Reviews*, vol. 121, no. 20, pp. 12465–12547, 2021, doi: 10.1021/acs.chemrev.1c00218.

[4] Y. Mochizuki, H.-J. Sung, A. Takahashi, Y. Kumagai, and F. Oba, “Theoretical exploration of mixed-anion antiperovskite semiconductors M_3XN (M = Mg, Ca, Sr, Ba; *X* = P, As, Sb, Bi),” *Physical Review Materials*, vol. 4, no. 4, p. 044601, 2020, doi: 10.1103/PhysRevMaterials.4.044601.

[5] D. Kalita, P. Sahu, and U. Manju, “Anti-perovskites for photovoltaics: materials development and challenges,” *Journal of Physics D: Applied Physics*, vol. 57, no. 34, p. 343002, 2024, doi: 10.1088/1361-6463/ad4daf.

[6] K. Haddadi, A. Bouhemadou, L. Louail, and S. Bin-Omran, “Inverse-perovskite oxides with , Ge, Sn, Pb: Structural, elastic and thermal properties,” *Solid State Communications*, vol. 150, no. 41–42, pp. 1995–2000, 2010, doi: 10.1016/j.ssc.2010.08.021.

[7] X. He *et al.*, “Inverse-Perovskite Ba_3BO (*B* = Si and Ge) as a High Performance Environmentally Benign Thermoelectric Material with Low Lattice Thermal Conductivity,” *Advanced Science*, vol. 11, no. 10, 2024, doi: 10.1002/advs.202307058.

[8] M. Hichour *et al.*, “FP-APW+lo study of the elastic, electronic and optical properties for the cubic antiperovskite $ANSr_3$ (A = As, Sb and Bi) under pressure effect,” *Physica B: Condensed Matter*, vol. 405, no. 7, pp. 1894–1900, 2010, doi: 10.1016/j.physb.2010.01.069.

[9] Y. Kang and S. Han, “Antiperovskite Oxides as Promising Candidates for High-Performance Ferroelectric Photovoltaics: First-Principles Investigation on Ba_4As_2O and Ba_4Sb_2O,” *ACS Applied Materials & Interfaces*, vol. 12, no. 39, pp. 43798–43804, 2020, doi: 10.1021/acsami.0c13034.

[10] M. Hassan, A. Shahid, and Q. Mahmood, “Structural, electronic, optical and thermoelectric investigations of antiperovskites A_3SnO (A = Ca, Sr, Ba) using density functional theory,” *Solid State Communications*, vol. 270, pp. 92–98, 2018, doi: 10.1016/j.ssc.2017.11.019.

[11] Q. Mahmood, A. Ashraf, and M. Hassan, “Investigations of optical and thermoelectric response of direct band gap Ca_3XO (X = Si, Ge) anti-perovskites stabilized in cubic and orthorhombic phases,” *Indian Journal of Physics*, vol. 92, no. 7, pp. 865–874, 2018, doi: 10.1007/s12648-018-1177-5.

[12] X. Li, Y. Zhang, W. Kang, Z. Yan, Y. Shen, and J. Huo, “Anti-perovskite nitrides and oxides: Properties and preparation,” *Computational Materials Science*, vol. 225, p. 112188, 2023, doi: 10.1016/j.commatsci.2023.112188.

[13] H. M. Tahir Farid *et al.*, “Optoelectronic and thermoelectric properties of A_3AsN (A = Mg, Ca, Sr and Ba) in cubic and orthorhombic phase,” *Journal of Materials Research and Technology*, vol. 13, pp. 1485–1495, 2021, doi: 10.1016/j.jmrt.2021.05.032.

[14] J. P. Perdew, K. Burke, and M. Ernzerhof, “Generalized Gradient Approximation Made Simple,” *Physical Review Letters*, vol. 77, no. 18, pp. 3865–3868, 1996, doi: 10.1103/PhysRevLett.77.3865.

[15] S. J. Clark *et al.*, “First principles methods using CASTEP,” *Zeitschrift für Kristallographie - Crystalline Materials*, vol. 220, no. 5–6, pp. 567–570, 2005, doi: 10.1524/zkri.220.5.567.65075.

[16] G. K. H. Madsen and D. J. Singh, “BoltzTraP. A code for calculating band-structure dependent quantities,” *Computer Physics Communications*, vol. 175, no. 1, pp. 67–71, 2006, doi: 10.1016/j.cpc.2006.03.007.

[17] D. H. Chung and W. R. Buessem, “The Voigt-Reuss-Hill (VRH) Approximation and the Elastic Moduli of Polycrystalline ZnO, TiO_2 (Rutile), and α-Al_2O_3,” *Journal of Applied Physics*, vol. 39, no. 6, pp. 2777–2782, 1968, doi: 10.1063/1.1656672.

[18] J. Nuss, C. Mühle, K. Hayama, V. Abdolazimi, and H. Takagi, “Tilting structures in *inverse* perovskites, M_3TtO (*M* = Ca, Sr, Ba, Eu; *Tt* = Si, Ge, Sn, Pb),” *Acta Crystallographica Section B Structural Science, Crystal*

Engineering and Materials, vol. 71, no. 3, pp. 300–312, 2015, doi: 10.1107/S2052520615006150.

[19] B. Huang and J. D. Corbett, "Orthorhombic Inverse Perovskitic Ba_3TtO (Tt = Ge, Si) as Zintl Phases," Zeitschrift für anorganische und allgemeine Chemie, vol. 624, no. 11, pp. 1787–1790, 1998, doi: https://doi.org/10.1002/(SICI)1521-3749(1998110)624:11<1787::AID-ZAAC1787>3.0.CO;2-P.

[20] A. Velden and M. Jansen, "Zur Kenntnis der inversen Perowskite M_3TO (M = Ca, Sr, Yb; T = Si, Ge, Sn, Pb)," *Zeitschrift für anorganische und allgemeine Chemie*, vol. 630, no. 2, pp. 234–238, 2004, doi: 10.1002/zaac.200300313.

[21] W. Peng and A. Zevalkink, "Limits of Cation Solubility in AMg_2Sb_2 (A = Mg, Ca, Sr, Ba) Alloys," *Materials*, vol. 12, no. 4, p. 586, 2019, doi: 10.3390/ma12040586.

[22] R. S. Mulliken, "Electronic Population Analysis on LCAO–MO Molecular Wave Functions. I," *The Journal of Chemical Physics*, vol. 23, no. 10, pp. 1833–1840, 1955, doi: 10.1063/1.1740588.

[23] B. Amin, I. Ahmad, M. Maqbool, S. Goumri-Said, and R. Ahmad, "*Ab initio* study of the bandgap engineering of $Al_{1-x}Ga_xN$ for optoelectronic applications," *Journal of Applied Physics*, vol. 109, no. 2, 2011, doi: 10.1063/1.3531996.

[24] A. C. Garcia-Castro, R. Ospina, and J. H. Quintero, "Octahedral distortion and electronic properties of the antiperovskite oxide Ba3SiO: First principles study," *Journal of Physics and Chemistry of Solids*, vol. 136, p. 109126, 2020, doi: 10.1016/j.jpcs.2019.109126.

[25] J.-H. Pöhls and A. Mar, "Thermoelectric properties of inverse perovskites A_3TtO (A = Mg, Ca; Tt = Si, Ge): Computational and experimental investigations," *Journal of Applied Physics*, vol. 126, no. 2, 2019, doi: 10.1063/1.5095247.

[26] A. Ahmed Adllan and A. Dal Corso, "Ultrasoft pseudopotentials and projector augmented-wave data sets: application to diatomic molecules," *Journal of Physics: Condensed Matter*, vol. 23, no. 42, p. 425501, 2011, doi: 10.1088/0953-8984/23/42/425501.

[27] D. A. Papaconstantopoulos and W. E. Pickett, "Ternary nitrides $BiNCa_3$ and $PbNCa_3$: Unusual ionic bonding in the antiperovskite structure," *Physical Review B*, vol. 45, no. 8, pp. 4008–4012, 1992, doi: 10.1103/PhysRevB.45.4008.

[28] A. Mehdizadeh Dehkordi, M. Zebarjadi, J. He, and T. M. Tritt, "Thermoelectric power factor: Enhancement mechanisms and strategies for higher performance thermoelectric materials," *Materials Science and Engineering: R: Reports*, vol. 97, pp. 1–22, 2015, doi: 10.1016/j.mser.2015.08.001.

[29] S. Zhang, B. Xu, Y. Lin, C. Nan, and W. Liu, "First-principles study of the layered thermoelectric material TiNBr," *RSC Advances*, vol. 9, no. 23, pp. 12886–12894, 2019, doi: 10.1039/C9RA00247B.

[30] D. M. Hoat, "Structural, optoelectronic and thermoelectric properties of antiperovskite compounds Ae_3PbS (Ae = Ca, Sr and Ba): A first principles study," *Physics Letters A*, vol. 383, no. 14, pp. 1648–1654, 2019, doi: 10.1016/j.physleta.2019.02.013.

[31] S. Naz, Z. Ali, S. Mehmood, I. Khan, and I. Ahmad, "Spin-orbit coupling effect on the optoelectronic and thermoelectric properties of the perovskites A_3SnO (A = Ca, Sr and Ba)," *Materials Science in Semiconductor Processing*, vol. 132, p. 105905, 2021, doi: 10.1016/j.mssp.2021.105905.

[32] M. Moakafi, R. Khenata, A. Bouhemadou, F. Semari, A. H. Reshak, and M. Rabah, "Elastic, electronic and optical properties of cubic antiperovskites $SbNCa_3$ and $BiNCa_3$," *Computational Materials Science*, vol. 46, no. 4, pp. 1051–1057, 2009, doi: 10.1016/j.commatsci.2009.05.011.

[33] S. Hasan, S. San, K. Baral, N. Li, P. Rulis, and W.-Y. Ching, "First-Principles Calculations of Thermoelectric Transport Properties of Quaternary and Ternary Bulk Chalcogenide Crystals," *Materials*, vol. 15, no. 8, p. 2843, 2022, doi: 10.3390/ma15082843.

[34] D. Han *et al.*, "Discovery of multi-anion antiperovskites X_6NFSn_2 (X = Ca, Sr) as promising thermoelectric materials by computational screening," *Matter*, vol. 7, no. 1, pp. 158–174, 2024, doi: 10.1016/j.matt.2023.10.022.

[35] S. Iqbal *et al.*, "Electronic and Optical Properties of Ca_3MN (M = Ge, Sn, Pb, P, As, Sb and Bi) Antiperovskite Compounds," *Journal of Electronic Materials*, vol. 45, no. 8, pp. 4188–4196, 2016, doi: 10.1007/s11664-016-4563-9.

[36] L.O Agbolade *et al.*, "Revisiting the Optoelectronic Properties of Graphene: A DFT Approach," *International Journal of Nanoelectronics and Materials (IJNeaM)*, vol. 17, no. 1, pp. 76–85, 2024, doi: 10.58915/ijneam.v17i1.476.

[37] S. V. H. Khosravi, M. Ilkhani, and M. Pashangpour, "Ab initio study of structural, electronic, and optical properties of the anti-perovskite compound Na_3OCN," *Chinese Journal of Physics*, vol. 89, pp. 1841–1851, 2024, doi: 10.1016/j.cjph.2023.05.015.

[38] Y. Benkrima, S. Benhamida, and D. Belfennache, "Theoretical study of structural and optical properties of ZnO in wurtzite phase," *Digest Journal of Nanomaterials and Biostructures*, vol. 18, no. 1, pp. 11–19, 2023, doi: 10.15251/DJNB.2023.181.11.

[39] A. Rahman, A. Rahman, and Z. Rahaman, "First-Principles Calculations of Structural, Electronic and Optical Properties of $HfZn_2$," *Journal of Advanced Physics*, vol. 5, no. 4, pp. 354–358, 2016, doi: 10.1166/jap.2016.1278.

[40] F. Lahourpour, A. Boochani, S. S. Parhizgar, and S. M. Elahi, "Structural, electronic and optical properties of graphene-like nano-layers MoX_2(X:S,Se,Te): DFT study," *Journal of Theoretical and Applied Physics*, vol. 13, no. 3, pp. 191–201, 2019, doi: 10.1007/s40094-019-0333-4.

[41] H. J. Lee, M. M. A. Gamel, P. J. Ker, M. Z. Jamaludin, Y. H. Wong, and J. P. R. David, "Absorption Coefficient of Bulk III-V Semiconductor Materials: A Review on Methods, Properties and Future Prospects," *Journal of*

Electronic Materials, vol. 51, no. 11, pp. 6082–6107, 2022, doi: 10.1007/s11664-022-09846-7.

[42] T.-B. Song *et al.*, “Perovskite solar cells: film formation and properties,” *Journal of Materials Chemistry A*, vol. 3, no. 17, pp. 9032–9050, 2015, doi: 10.1039/C4TA05246C.

[43] R. Islam, M. M. Hossain, M. A. Ali, M. M. Uddin, and S. H. Naqib, “Metallic boro-carbides of A_2BC (A = Ti, Zr, Hf and W): a comprehensive theoretical study for thermo-mechanical and optoelectronic applications,” *RSC Advances*, vol. 12, no. 51, pp. 32994–33007, 2022, doi: 10.1039/D2RA05448E.

[44] S. J. Hong, J. H. Lee, D. Gelija, and W. J. Chung, “Refractive-index Prediction for High-refractive-index Optical Glasses Based on the B_2O_3-La_2O_3-Ta_2O_5-SiO_2 System Using Machine Learning,” *Current Optics and Photonics*, vol. 8, no. 3, pp. 230–238, 2024.